UNIVERSITY OF OSLO
Department of Informatics

Adaptive Beamforming for Active Sonar Imaging

Ann E. A. Blomberg

October 18, 2011

Series of dissertations submitted to the
Faculty of Mathematics and Natural Sciences, University of Oslo
No. 1161

ISSN 1501-7710

Cover: Inger Sandved Anfinsen.
Printed in Norway: AIT Oslo AS.

Produced in co-operation with Unipub.
The thesis is produced by Unipub merely in connection with the
thesis defence. Kindly direct all inquiries regarding the thesis to the copyright
holder or the unit which grants the doctorate.

Preface

This thesis has been submitted to the Faculty of Mathematics and Natural Sciences at the University of Oslo in partial fulfillment of the requirements for the degree *Philosophiae Doctor (Ph.D.)*. The work was carried out at the Digital Signal Processing and Image Analysis group at the Department of Informatics, University of Oslo. During 2009-2010 I had the pleasure of spending seven months at the University of Canterbury, New Zealand. This work has been supervised by Associate Professor Andreas Austeng, Adjunct Associate Professor Roy Edgar Hansen and Professor Sverre Holm. The work is part of the KMB project "High Resolution Imaging and Beamforming", financed by the Norwegian Research Council and Kongsberg Maritime.

Acknowledgements

I would like to start by expressing my sincere gratitude to my supervisors, Associate Professor Andreas Austeng, Adjunct Associate Professor Roy E. Hansen, and Professor Sverre Holm. Andreas Austeng has been a constant source of motivation, constructive feedback, patience and positivity throughout my time as a PhD student. I am also grateful to Roy E. Hansen for his enthusiasm and commitment, and for always finding the time for discussions, and to review and comment on my work. I also thank Kongsberg Maritime for a fruitful cooperation, and for providing experimental data.

Dr. Michael Hayes and Professor Peter Gough at the University of Canterbury, New Zealand, deserve a special thanks for welcoming me as a guest researcher for seven months. Dr. Michael Hayes not only provided data and constructive input to my work, he also helped me find my place and feel at home in New Zealand.

I would also like to thank my colleagues at the DSB-group for providing such a motivating and pleasant working environment. My family and friends also deserve my gratitude for their patience and encouragement. Most of all, I thank Sinan for his patience, support, and love.

Abstract

This thesis addresses the use of adaptive beamforming and imaging methods applied to active sonar. While adaptive beamformers are known to offer improved performance when applied to *passive* sonars, their use is limited in active sonar systems. In this thesis, we investigate the potential performance gains of using adaptive beamforming methods for a range of active sonar applications. Key challenges that are addressed include coherent signals, arbitrary array geometries, computational load, and robustness. We also investigate the use of aperture coherence, or coherence over the elements of the receiver array, for improved sonar imaging. We conclude that in many cases, improved image quality is obtained by using adaptive beamforming methods. Noise, particularly directive noise such as sidelobe energy, is suppressed, edges of objects appear sharper and image resolution is improved. The minimum variance distortionless response (MVDR) beamformer offers superior resolution capabilities as well as the ability to suppress noise and interference, but requires robustification techniques in order to perform well in an active sonar setting. The amplitude and phase estimation (APES) beamformer is robust and displays similar noise and interference suppression capabilities as the MVDR, but somewhat lower resolution. The low complexity adaptive (LCA) beamformer offers much of the same improvements as the fully adaptive MVDR at a fraction of the computational cost, is robust, and is particularly well suited for small arrays. The coherence factor and the closely related scaled Wiener postfilter represent a promising class of adaptive imaging methods that work in a fundamentally different way than the MVDR and APES beamformers. Based on the concept that noise and interference appear more random across the receiver array than the echo from a reflecting object, they effectively attenuate noisy image pixels in an adaptive way, resulting in images which appear less contaminated by noise. As a result, shadow regions are enhanced and details in the image appear more clearly defined.

List of Publications

This thesis is based on the following five papers, referred to in the text by their Roman numerals (I-V).

I A. E. A. Blomberg, I. K. Holfort, A. Austeng, J.-F. Synnevåg, S. Holm and J. A. Jensen, "APES beamforming applied to medical ultrasound imaging", *Proc. IEEE Ultrasonics symposium*, Rome, 2009.

II A. E. A. Blomberg, A. Austeng and R. E. Hansen, "Adaptive beamforming applied to a cylindrical sonar array using an interpolated array transformation", *IEEE Journal of Oceanic Engineering*. Accepted for publication Sep. 14, 2011.

III A. E. A. Blomberg, A. Austeng, R. E. Hansen and S. A. V. Synnes, "Improving sonar performance in shallow water using adaptive beamforming", *IEEE Journal of Oceanic Engineering.* Revised version submitted Aug. 30, 2011.

IV A. E. A. Blomberg, R. E. Hansen, S. A. V. Synnes and A. Austeng, "Improved interferometric sonar performance in shallow water using adaptive beamforming", *Proceedings of underwater acoustic measurements (UAM)*, Kos, Greece, June 2011.

V A. E. A. Blomberg, C.-I. C. Nilsen, A. Austeng and R. E. Hansen, "Adaptive sonar imaging using aperture coherence", *IEEE Journal of Oceanic Engineering.* Submitted Oct. 1, 2011.

Related publications

i A. E. A. Blomberg, A. Austeng, R. E. Hansen, S. Holm, "Minimum variance adaptive beamforming applied to a circular sonar array", *Proceedings of underwater acoustic measurements (UAM)*, Nafplion, Greece, June 2009.

ii A. E. A. Blomberg and M. Hayes, "Multipath reduction for bathymetry using adaptive beamforming", *IEEE OCEANS conf. proc.*, Sydney, May 2010.

Contents

Chapter 1

Introduction

1.1 Aims of this thesis

Adaptive beamforming methods have existed for decades, but are not as of today extensively used for active sonar imaging. The aim of the work presented in this thesis has been to investigate the use of adaptive beamforming methods for active sonar systems, and to analyze the potential performance gains offered by adaptive methods, as well as their limitations.

1.2 Motivation and scope

As of today, sonar imaging is the most effective means of documenting the subsea environment. While optical cameras offer superb image quality when operating in air, they have limited capabilities under water since the electromagnetic waves are quickly attenuated in this medium. The alternative is to rely on sound waves. Sound waves are much less affected by attenuation in water, and the relatively low frequencies used in sonar enable the waves to travel far. However, the low frequencies also have a negative impact on the obtainable image resolution.

This thesis was motivated by the desire to obtain high quality, noise-free, high-resolution images using sonar. Today, active sonar systems generally use conventional delay-and-sum (DAS) beamforming methods for imaging. Conventional beamformers are robust and simple, but they leave many of the challenges of sonar imaging unresolved. Sonar images are often degraded by noise, and the image resolution as well as the range at which useful images can be obtained is limited. The goal of an adaptive beamformer in this context is to improve the image quality as well as the obtainable sonar range. This is achieved by allowing the beamformer to *adapt* to the situation, recognizing sources of noise and interference and suppressing them before they have the chance to contaminate the image. The desired result is an image containing more useful and correct information, less noise, and improved image resolution.

The scope of this thesis has been to evaluate the feasibility and possible performance gains of using adaptive methods for active sonar imaging. Focus has been on investigating how different adaptive methods can be implemented in a practical setting, and to analyze their performance as well as to address key challenges. Two of the most common adaptive beamforming methods, the minimum variance distortionless response (MVDR) and the amplitude and phase estimation (APES) beamformers, are considered, as well as a low complexity variant of the adaptive MVDR beamformer. Adaptive imaging methods based on aperture coherence represent a promising class of adaptive methods, and are also considered.

The focus in this thesis is on sidescan and sectorscan sonars. The work is heavily anchored in real-world applications, and experimental data from three different operational sonar systems is used. The extension of adaptive methods to synthetic aperture sonar (SAS) is suggested as a topic for further research.

1.3 Thesis outline

Chapter 2 covers essential background material related to paper I through V. We start by offering a brief introduction to sonar and sonar imaging in 2.1, and to the propagation of sound waves in 2.2. Chapter 2.3 considers array signal processing and conventional beamforming, and 2.4 covers adaptive beamforming as well as adaptive imaging based on aperture coherence. Chapter 2.5 addresses the interesting but non-trivial question of how to determine the quality of an image. Chapter 3 summarizes each of the papers included in this thesis. Chapter 4 lists the main contributions of this thesis, and a case study comparing the proposed imaging methods discussed in papers I-V is included for completeness. Suggestions for future work are offered in chapter 5. Papers I to V are included sequentially after chapter 5.

Chapter 2

Background

This chapter offers a brief introduction to the concepts of sonar imaging, as well as basic theory on array signal processing including conventional and adaptive beamforming methods. The theory covered is not exhaustive, but is intended to provide the reader with sufficient background information for the papers included in this thesis.

2.1 Sonar

2.1.1 A historical perspective

Sonar is an abbreviation for SOund Navigation And Ranging, and is a technique that uses the propagation of sound waves either to gain knowledge about the surroundings, or to convey information. Sonar is used mainly underwater. The fact that sound waves travel easily in water has been known for thousands of years. The first sonar systems were *passive*, meaning that no sound waves were transmitted. A passive system "listens" to its surroundings and uses the sound waves measured by the receiver to gain information about the source. Leonardo da Vinci is often mentioned as one of the early inspirations for passive sonars. In 1490, he made the following observation [1]:

> "If you cause your ship to stop, and place the head of a long tube in the water and place the outer extremity to your ear, you will hear ships at a great distance from you."

It was not until more than 400 years later, in 1906, that the first practical passive sonar system was invented by naval architect Lewis Nixon. The purpose of Nixon's listening device was to detect ice bergs. The interest in the field of passive sonar for detection of obstacles was spurred by the sinking of the Titanic in 1912. Later the same year, the Canadian engineer Reginald Fessenden built an experimental system and demonstrated its use for echo ranging and underwater communication using Morse code. In 1915, Paul Langévin invented the first passive sonar system used for submarine detection. Soon after, *active* sonar systems emerged. An active sonar transmits a sound wave, or pulse, into the water and uses the returned echo to gain information about the environment. During and between the first and second World Wars, a great deal of research was conducted on passive and active sonar systems for military purposes such as submarine detection and localization, and underwater communication. A brief historical overview of the use of sonar is given in [2, Chapter1].

Today, sonars are widely used in military as well as civilian applications. Commercial vessels and many recreational boats use sonars for navigation and depth estimation. In the fishery industry, sonars are used for detecting and localizing schools of fish, and for biomass estimation. Sonar systems are used by the scientific community for instance to map the amount of fish and the movement of fish in the oceans, and to obtain images of natural and man-made objects on the seafloor. Diver detection devices can be used to avoid collisions and to detect and track underwater threats. Sub-bottom profilers operate at low enough frequencies to penetrate into the upper layer of the seafloor, thereby revealing its characteristics. Different types of sonars and their applications are nicely covered in [3], and [4] offers an overview of the past, present, and future of underwater acoustic signal processing methods.

Figure 2.1: Basic processing flow for an active sonar imaging system.

2.1.2 Sonar imaging

This thesis considers mainly sonar *imaging* systems. The objective of a sonar imaging system is to create an image either of an object in the water column such as a school of fish or a construction, or of the seafloor. Ideally, these images should be of high resolution, noise free, and correctly represent the scene. Sonar imaging systems can be divided into several categories, including sidescan sonars, sectorscan sonars, interferometric sonars, and synthetic aperture sonars (SAS). The applications and processing details vary, but the basic processing flow is the same for all of these systems. The basic processing flow for an active sonar imaging system is illustrated by Figure 2.1.

The first step is optional pre-processing of the received data. The pre-processing may include removal of data from defective sensors and Doppler compensation to compensate for movement of the sonar during reception. If the transmitted pulse was a coded pulse such as the commonly used chirp, matched filtering is applied on reception to increase the signal-to-noise ratio (SNR) and to compress the pulse in range [6]. Finally, beamforming is used to create the output image. Processing of sonar data is thoroughly covered in for example [7], and beamforming for sonar is covered in several textbooks, including [8].

Figure 2.2 illustrates the imaging geometry for a sidescan sonar system. A sidescan sonar uses the motion of the sonar to image an area of interest. As the sonar travels, it transmits pulses, or *pings* either to one side or to both sides of the sonar. On reception, one scanline or a few scanlines are formed around broadside. The scanlines are arranged side by side to form a two-dimensional output image. Sidescan sonars are widely used since they offer an efficient way

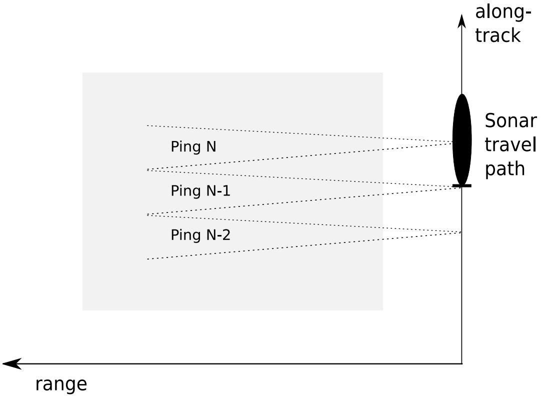

Figure 2.2: Imaging geometry for a sidescan imaging system. A two-dimensional image is created by forming one or a few scanlines around broadside for each transmitted ping.

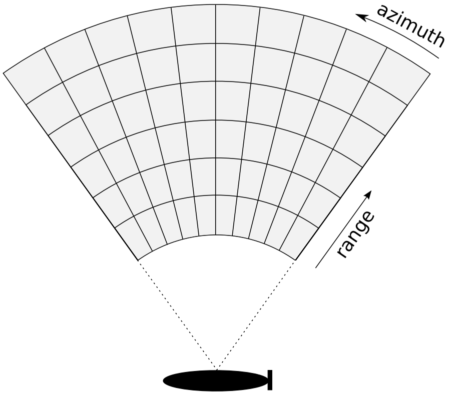

Figure 2.3: Imaging geometry in a sectorscan imaging system. For a single transmitted ping, the receiver is steered consecutively in many directions, creating a two-dimensional image from a single ping. Adapted from [5].

of imaging large areas and they generally require simple hardware components. Sidescan sonar systems are covered in for example [9] and [10].

A sectorscan sonar creates a two-dimensional image from a single transmission by scanning over a range of angles. The scanning can be implemented using phase shifts to delay the signals received by each element, consecutively *steering* the receiver in different directions. Sectorscan is common for instance in fishery sonar, where a 360-degree field-of-view is desired.

The objective of an interferometric sonar is to estimate the height variations within an area of interest. An interferometric sonar uses two or more vertically displaced receivers, and estimates the height of a reflecting object using the difference in arrival times of the signals measured by the receivers. Interferometry is well documented in the radar literature, for instance in [6] and [11]. In [12], interferometry for SAS is covered.

In a conventional sidescan or sectorscan imaging system, the obtainable azimuth resolution (also referred to as along-track resolution or angular resolution) is directly related to the size

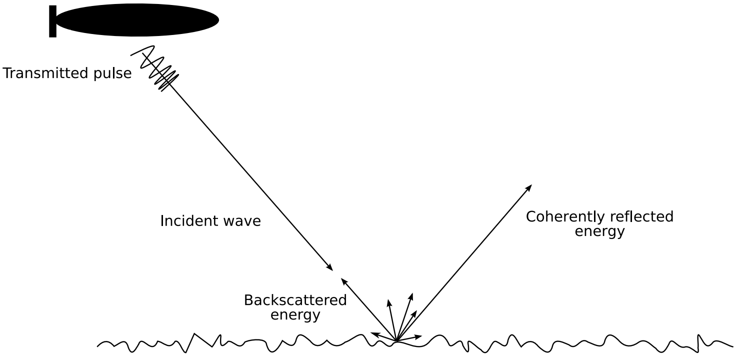

Figure 2.4: Scattering and reflection from a rough surface.

of the receiver array. The larger the array, the better the resolution. SAS is a relatively new technique that synthesizes a large receiver array by combining data from several pings as the sonar travels along its path. SAS processing results in a drastic improvement in the obtainable image resolution. An introduction to SAS imaging is given in [5].

2.1.3 Scattering and reflection

In sonar imaging, a pulse is transmitted, and the returned echo is used to estimate the reflectivity of a region of interest. Each time the transmitted pulse interacts with an object or a surface, the energy in the wavefield is *scattered*. Figure 2.4 illustrates how the incident wavefield may be scattered when encountering a rough surface such as the seafloor. Part of the energy is *coherently reflected*, and continues to propagate at an angle given by Snell's law. Part of the energy is scattered in different directions, depending on the properties of the surface. The part of the scattered field that is directed back toward the sonar is referred to as the *backscattered* part. In a monostatic sonar system, i.e., where the transmitter and receiver are co-located, it is the backscattered field that is recorded and used. How much of the transmitted energy that is returned toward the sonar is described by acoustic scattering theory, and is a function of the wavelength of the transmitted pulse, the roughness and other physical properties of the scattering object or surface, as well as the angle of incidence. An introduction to acoustic scattering and reflection from rough surfaces is given in [3, Chapter 3]. The interested reader is also referred to [13], [14, Chapter 7], and [15].

2.1.4 Key challenges in sonar imaging

In an ideal situation of a flat seafloor and a homogeneous medium with constant propagation speed, no interfering signals or noise, and no multipath propagation, sonar imaging would be a simple task. However, the subsea environment is complex, and obtaining high-quality images is far from trivial [2].

The fact that sound waves travel easily in water is a blessing as well as a curse. It allows sonars to detect a school of fish several kilometres away, or to passively detect a submarine at a large distance. But it also means that noise from ships, waves, and seismic activity travels far and stays in the water for a long period of time. Ambient noise, or background noise, can be caused by many factors including waves, rain, wind, ships, and noise made by shrimp and other animals. Ambient noise is a more or less constant and spatially white source of noise. Ship noise or seismic activity often manifests itself as a directional source of interference. The amount of noise in the water makes the task of detecting signals of interest and separating them from the noise and interference a challenge. It also sets a lower limit on the intensity of acoustic signals from which useful information can be obtained [2, Chapter 10], [16, Chapter 7].

The complex topography of the seafloor is also a major challenge. Height variations caused by for example submerged mountain ranges cause geometrical distortions in a sonar image. Another issue is multipath propagation, where the transmitted pulse has a travel path which deviates from the direct path from the transmitter to the reflecting object and back to the receiver. As a result, there may be two or more signals impinging on the receiver array at any instant. Multipath propagation causes image artifacts such as "ghost" reflections in the image. It also reduces the SNR, in practice limiting the achievable range of the sonar. Variations in water temperature, salinity, currents, vegetation and differences in sediment types cause further challenges.

2.2 Propagating sound waves

A common denominator amongst radar, seismic imaging, mobile communications, medical ultrasound, and sonar, is the use of propagating waves. Radar uses electromagnetic waves for detection and imaging, while seismics, medical ultrasound systems and sonars make use of sound waves, or acoustic pressure waves. Key differences between the different acoustic imaging systems are the frequency of the transmitted signal, and the speed of propagation.

An acoustic wave with frequency f propagating through a medium with propagation speed c has a wavelength given by $\lambda = c/f$. The obtainable azimuth resolution is proportional to the wavelength, λ. Thus high frequencies yield higher azimuth resolution. However, high frequencies are attenuated more than lower frequencies, limiting the distance a high-frequent wave can travel. In seismic imaging, the transmitted frequencies are low (typically in the range 5 to 100 Hz) in order to penetrate the layers of the earth. In medical ultrasound imaging the waves do not need to propagate far, so frequencies in the MHz region are used for high resolution images. Sonar systems operate at frequencies ranging from less than 1 kHz to several hundred kHz, depending on the application. A fish finding sonar typically operates at 20-30 kHz in order to locate fish several kilometres away, while a sidescan sonar designed to detect small objects on the seafloor may operate at over 100 kHz.

The *wave equation* is a second-order partial differential equation used to describe the propagating wavefield. Acoustic pressure waves originate from local compression and dilation of a medium. The propagation of an acoustic pressure wave, $s(x, y, z, t)$, in a gas or fluid, can be described using the wave equation:

$$\frac{\partial^2 s}{\partial x^2} + \frac{\partial^2 s}{\partial y^2} + \frac{\partial^2 s}{\partial z^2} = \frac{1}{c^2}\frac{\partial^2 s}{\partial t^2}, \tag{2.1}$$

where (x, y, z) represents a position in a three-dimensional space and t denotes the time. One solution to (2.1) in a constant sound speed medium is a monochromatic plane wave:

$$s(\mathbf{p}, t) = Ae^{j(\omega t - \mathbf{k}^T\mathbf{p})}, \tag{2.2}$$

where the vector **p** denotes the spatial position, (x, y, z), A is the signal amplitude, and $\omega = 2\pi f$ is the frequency measured in radians per second. The wavenumber vector, $\mathbf{k} = (k_x, k_y, k_z)$, describes the direction in which the wave is propagating, and $k = |\mathbf{k}| = \frac{2\pi}{\lambda}$ is the wavenumber. Another solution to 2.1 is a spherical wave:

$$s(r, t) = \frac{A}{r}e^{j(\omega t - kr)}, \tag{2.3}$$

where r denotes the radius in spherical coordinates from the source. When the source is in the farfield of the receiver, a spherical wavefront appears to the receiver as a plane wave. The wave equation is derived in for example [15, Chapter 2].

2.3 Array processing and beamforming

The transmitter/receiver can consist of a single element, or of an array of elements configured in some structure. The use of an array makes *beamforming* possible, on transmission as well as on reception. Common array structures include uniformly sampled linear arrays (ULAs), rectangular arrays, circular, spherical, and cylindrical arrays. The structure is chosen according to the application needs. Beamforming may be used to focus the transmitted beam, and to steer it in a desired direction. Similarly, beamforming on the receiver side can be used to control the array response and to increase the output SNR. The improvement in output SNR when using an array, compared to a single, omnidirectional receiver, is referred to as the *array gain*. Assuming spatially white noise, the array gain of an M-element array is proportional to M.

2.3.1 Signal model

We assume an array of M elements with (x, y, z) positions described by the position vector **p**, and a monochromatic plane wave of the form (2.2) impinging on the array. The wavefield received by element m at time sample n can then be expressed as

$$s_m[n] = Ae^{j(\omega n - \mathbf{k}^T\mathbf{p}_m)}. \tag{2.4}$$

The signal amplitude, A, is directly related to the reflectivity of the scattering object. In vector notation, **s** can be written as

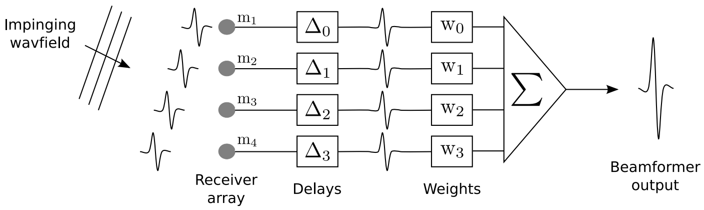

Figure 2.5: Schematic illustration of a DAS beamformer for a four-element receiver array. When steering toward the impinging wavefield, a delay is applied such that the measured signals line up in phase, before weighting and combining them to form the beamformer output.

$$\mathbf{s}[n] = \begin{bmatrix} s_0[n] \\ s_1[n] \\ . \\ . \\ s_{M-1}[n] \end{bmatrix} = \begin{bmatrix} Ae^{j(\omega n - \mathbf{k}^T\mathbf{p}_0)} \\ Ae^{j(\omega n - \mathbf{k}^T\mathbf{p}_1)} \\ . \\ . \\ Ae^{j(\omega n - \mathbf{k}^T\mathbf{p}_{M-1})} \end{bmatrix} = Ae^{j\omega n}\mathbf{a}(\mathbf{k}),$$

where **a** is the *steering vector* defined as

$$\mathbf{a}(\mathbf{k}) = \begin{bmatrix} e^{-j\mathbf{k}^T\mathbf{p}_0} \\ e^{-j\mathbf{k}^T\mathbf{p}_1} \\ . \\ . \\ e^{-j\mathbf{k}^T\mathbf{p}_{M-1}} \end{bmatrix}.$$

The total wavefield measured by the receiver array generally consists of a signal part, **s**[n], and a noise-and-interference part, **n**[n]. We can write the data measured by the array at time sample n as

$$\mathbf{x}[n] = \mathbf{s}[n] + \mathbf{n}[n]. \tag{2.5}$$

We assume that the signal $\mathbf{s}[n]$ is un-correlated with the noise and interference, $\mathbf{n}[n]$.

2.3.2 Conventional beamforming

Beamforming involves steering the beam by delaying the measurements at each sensor such that the signals line up in phase, and then performing a weighted combination of the delayed measurements to form the beamformer output [8]. The simplest and as of today the most common beamformer is the conventional delay-and-sum (DAS) beamformer. In the sonar and radar literature it is also referred to as *backprojection*. In conventional, non-adaptive beamformers, the weights applied to each sensor are pre-defined and data-independent. The weights can be uniform, or defined by a window function such as a Hanning or a Kaiser window [17, Chapter 3]. Figure 2.5 illustrates how a conventional DAS beamformer works on the receiver side.

In an imaging context, receive beamforming is used to focus the receive beam to each pixel in the output image. The desired signal is the part of the backscattered field originating from the point in space represented by that pixel. The delays are computed to compensate for the travel time from the transmitter, to the pixel of interest, and back to each receiver element.

Given an array of M sensors, the output of a general beamformer at time sample n can be written as

$$z\left[n\right] = \sum_{m=0}^{M-1} w_m^*[n] x_m\left[n - \Delta_m[n]\right], \tag{2.6}$$

where $x_m[n - \Delta_m[n]]$ is the received signal at element m delayed by $\Delta_m[n]$, w_m refers to the weight applied to sensor m, and * denotes the complex conjugate operator. The weights in a conventional beamformer are static and generally real-valued, defining only an amplitude shading over the array. The $(^*)$ and the time dependence is included here since (2.6) is valid also for the adaptive beamformers described in Chapter 2.4, where the weights may be complex-valued and vary as a function of time.

2.3.3 The beampattern

The *beampattern* describes an array's response to an impinging wavefield as a function of direction of arrival (DOA). The far-field beampattern for the DAS beamformer is defined as

$$B(k) = \sum_{m=0}^{M-1} w_m^* e^{j\mathbf{k}^T\mathbf{p}_m}. \tag{2.7}$$

The beampattern for the nearfield can be computed by incorporating the expression for a spherical wavefront given by (2.3) instead of a plane wave as defined in (2.2).

Figure 2.6 shows the beampattern for the conventional DAS beamformer weighted using four common window functions. The beampattern of a conventional beamformer reveals several qualities of the beamformer, such as its resolution and noise suppression capabilities. The resolution is often defined as the -3dB width of the mainlobe. The sidelobe levels reveal how much signals arriving from directions other than the steering direction are attenuated, and the positions of the nulls dictate the angles at which interfering signals are rejected.

The main advantages of the conventional DAS beamformer are that it is simple, robust, and can be efficiently implemented. The sensor weights are pre-defined and static, although they can be designed to meet certain demands. If high resolution is of importance but sidelobe levels of -13 dB are acceptable, a rectangular window should be chosen (i.e., equal weighting applied to each sensor). If, on the other hand, noise reduction through sidelobe suppression is a priority, a window function such as a Hanning window (sometimes also referred to as a Hann window) may be used to control the sidelobe levels at the expense of a wider mainlobe. Whatever the choice, as long as the weights are static there is a tradeoff between resolution and sidelobe levels.

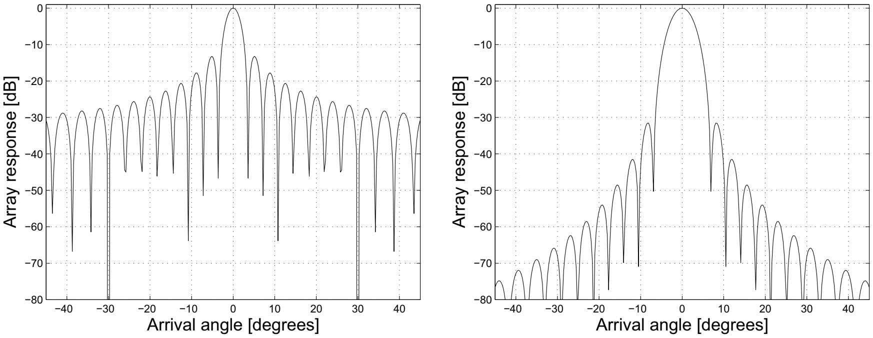

(a) Rectangular window

(b) Hanning window

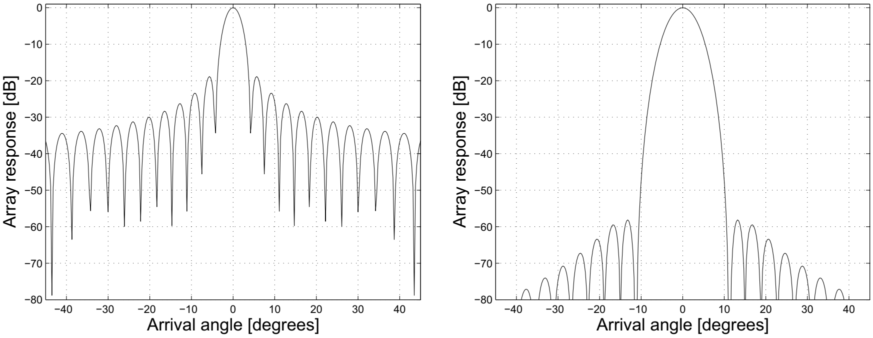

(c) Kaiser window, $\beta = 2$

(d) Blackman window

Figure 2.6: Example DAS beampatterns for a ULA weighted using four common window functions. Uniform weights are used in (a), Hanning weights in (b), Kaiser weights in (c), and Blackman weights in (d).

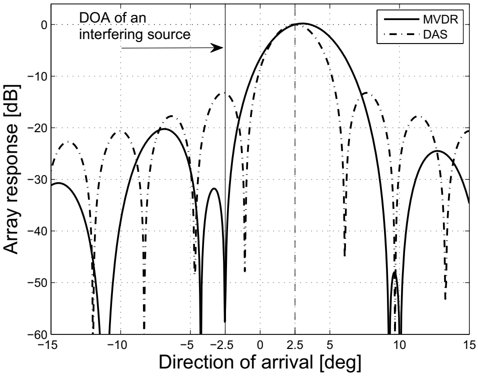

Figure 2.7: Beampattern for the MVDR and uniformly weighted DAS beamformers, respectively. When steering toward 2.5 degrees, the MVDR beamformer places a null in the direction of an interfering signal arriving from -2.5 degrees, while ensuring unit gain in the steering direction.

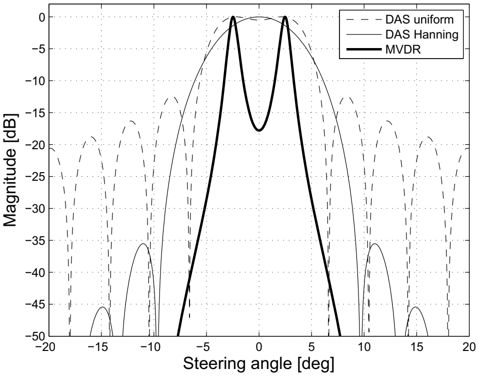

Figure 2.8: Steered response for the uniformly weighted DAS, the Hanning-weighted DAS, and the MVDR beamformers, respectively. In this scenario, one signal is arriving from -2.5 *degrees and another from* 2.5 *degrees.*

2.4 Adaptive beamforming

While conventional beamformers use pre-defined sensor weights, adaptive beamformers allow the sensor weights to change dynamically depending on the characteristics of the measured wavefield. For each pixel in the final image, a different set of weights may have been used. The weights are computed using an optimization criterion defined by the adaptive beamformer in question. In many cases, adaptive beamformers offer improved resolution and noise suppression compared to their non-adaptive counterparts [8, chapter 7], [18]. This improvement comes at the cost of added computational complexity.

Figure 2.7 shows an example beampattern for a conventional and an adaptive beamformer (the minimum variance distortionless response (MVDR) beamformer, described in Chapter 2.4.2), where the signal of interest is arriving from a DOA of 2.5degrees, while at the same time an interfering signal is arriving from a direction of -2.5 degrees. The conventional DAS beamformer is not aware of the interfering source, and the static beampattern determines how much it is suppressed. In this example, the interfering source has a DOA corresponding to the first sidelobe of the DAS beamformer. The adaptive beamformer calculates sensor weights such that a null is placed in the direction of the interfering source [17, Chapter 6].

The *steered response* is the beamformer output as a function of steering angle, for a given scenario. Figure 2.8 shows the steered response for the uniformly weighted and the Hanning-weighted DAS beamformers, and the adaptive MVDR beamformer. The scenario is the same as in Figure 2.7, with two signals arriving from -2.5 degrees and 2.5 degrees, respectively. In this case the ideal steered response is two narrow peaks showing the DOA and amplitude of the two signals. Both signals have an amplitude of 1 (0 dB). The two signals are not resolved at all by the Hanning-weighted DAS beamformer, and the uniformly weighted DAS beamformer displays only a slight dip between them. The adaptive beamformer clearly distinguishes two distinct peaks corresponding to the impinging signals.

Two of the most commonly used adaptive beamformers are the MVDR and the minimum power distortionless response (MPDR) beamformers. These two belong to the class of *distortionless* beamformers, meaning that they strive to fulfill some optimization criterion while ensuring unit gain in the direction of interest. In the following, we differentiate between the *optimal* MPDR and MVDR beamformers in an ideal case where all the statistics are known, and their adaptive implementations.

2.4.1 The optimal MPDR and MVDR beamformers

The optimal minimum *power* distortionless response (MPDR) beamformer computes the weight vector, $\mathbf{w}$, that minimizes the power of the beamformer output while ensuring unit gain in the direction of interest. This can be expressed as the following optimization problem:

$$\mathbf{w}_{\text{MPDR}} = \arg\min_{\mathbf{w}} E\left\{|z[n]|^2\right\} \text{ subject to } \mathbf{w}[n]^H\mathbf{a} = 1, \tag{2.8}$$

where z is the beamformer output defined by (2.6). Omitting the time dependence, the minimization problem in (2.8) can be re-written as

$$\begin{aligned} &\min_{\mathbf{w}} E\left\{|\mathbf{w}^H\mathbf{x}|^2\right\} \\ =&\min_{\mathbf{w}} E\left\{\mathbf{w}^H\mathbf{x}\mathbf{x}^H\mathbf{w}\right\} \\ =&\min_{\mathbf{w}} \mathbf{w}^H E\left\{\mathbf{x}\mathbf{x}^H\right\}\mathbf{w} \\ =&\min_{\mathbf{w}} \mathbf{w}^H\mathbf{R}\mathbf{w}, \text{ subject to } \mathbf{w}^H\mathbf{a} = 1, \end{aligned} \tag{2.9}$$

where $\mathbf{R} = E\left\{\mathbf{x}\,\mathbf{x}^H\right\}$ is the spatial data covariance matrix. The analytical solution to the MPDR beamformer can be found using Lagrange multipliers [17, Chapter 6], and is given by

$$\mathbf{w}_{\text{MPDR}} = \frac{\mathbf{R}^{-1}\mathbf{a}}{\mathbf{a}^H\mathbf{R}^{-1}\mathbf{a}}. \tag{2.10}$$

Equation (2.10) needs to be solved for each pixel in the output image.

The optimal minimum *variance* distortionless response (MVDR) beamformer computes the weights that minimize the variance of the beamformer output while ensuring unit gain in the direction of interest. Recall from chapter 2.3.1 that the data vector, $\mathbf{x}$, can be decomposed into a signal part, $\mathbf{s}$ and a noise and interference part, $\mathbf{n}$, such that the beamformer output can be written as

$$z = \mathbf{w}^H\mathbf{x} = \mathbf{w}^H(\mathbf{s}+\mathbf{n}). \tag{2.11}$$

While the optimal MPDR beamformer minimizes the power of the beamformer output, z, the optimal MVDR beamformer minimizes the power of the *noise-and-interference* part of the output. It can be expressed as the minimization problem

$$\begin{aligned} &\min_{\mathbf{w}} E\left\{|\mathbf{w}^H\mathbf{n}|^2\right\} \\ =&\min_{\mathbf{w}} E\left\{\mathbf{w}^H\mathbf{n}\mathbf{n}^H\mathbf{w}\right\} \\ =&\min_{\mathbf{w}} \mathbf{w}^H E\left\{\mathbf{n}\mathbf{n}^H\right\}\mathbf{w} \\ =&\min_{\mathbf{w}} \mathbf{w}^H\mathbf{Q}\mathbf{w}, \end{aligned} \tag{2.12}$$

where $\mathbf{Q}$ is the *noise-and-interference* covariance matrix. This problem has an analytical solution given by [17, Chapter 6]

$$\mathbf{w}_{\text{MVDR}} = \frac{\mathbf{Q}^{-1}\mathbf{a}}{\mathbf{a}^H\mathbf{Q}^{-1}\mathbf{a}}. \tag{2.13}$$

The MVDR solution given by (2.13) is similar in form to the MPDR solution in (2.10). In [19], the author shows that the two solutions are identical in the case of zero-mean noise-and-interference:

$$\min_{\mathbf{w}} \mathbf{w}^H\mathbf{R}\mathbf{w} = \min_{\mathbf{w}} \mathbf{w}^H(\mathbf{R}_s+\mathbf{Q})\mathbf{w} = \min_{\mathbf{w}} \mathbf{w}^H\mathbf{Q}\mathbf{w}, \tag{2.14}$$

where $\mathbf{R}_s$ contains the signal component of the data covariance matrix. The first equality holds because under the assumption of uncorrelated signal and noise, the spatial data covariance matrix can be written as

$$\mathbf{R} = E\left\{\mathbf{x}\,\mathbf{x}^H\right\} = E\left\{(\mathbf{s}+\mathbf{n})(\mathbf{s}+\mathbf{n})^H\right\} = \mathbf{R}_s + \mathbf{Q}. \tag{2.15}$$

The second equality holds because both beamformers are bound by the distortionless response constraint, which implies that the signal component of the output should not be distorted in any way. Note that the equivalence of these two solutions is only valid in the ideal case of known data statistics and noise which is uncorrelated with the signal. Their implementations differ, as seen in sections 2.4.2 and 2.4.3.

2.4.2 The adaptive MVDR beamformer

The difference between the *optimal* beamformers and their adaptive implementations arise because the statistics of the data are unknown, and $\mathbf{R}$ and $\mathbf{Q}$ need to be replaced by their estimates, $\hat{\mathbf{R}}$ and $\hat{\mathbf{Q}}$. The adaptive MVDR beamformer is also known as the Capon beamformer or simply the minimum variance (MV) beamformer. While the name suggests that it is an implementation of the optimal MVDR beamformer, it is actually an implementation of the optimal MPDR

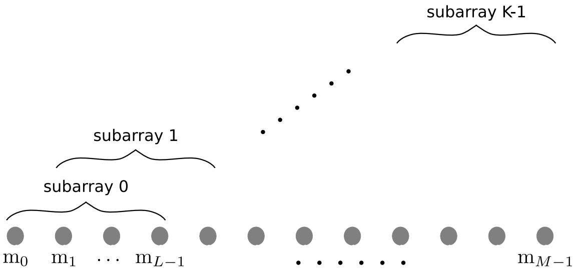

Figure 2.9: Subarray averaging implies dividing the receiver array into K overlapping subarrays of equal length, and computing the average of these.

beamformer. Although this can be confusing, we will stick to calling it the MVDR beamformer since this is common practice in the sonar literature.

The solution to the adaptive MVDR beamformer is [20]

$$\mathbf{w}_{\mathrm{MVDR}} = \frac{\hat{\mathbf{R}}^{-1}\mathbf{a}}{\mathbf{a}^H\hat{\mathbf{R}}^{-1}\mathbf{a}}. \tag{2.16}$$

A common estimator for the covariance matrix, **R**, is the sample covariance matrix :

$$\hat{\mathbf{R}} = \frac{1}{P}\sum_{p=0}^{P-1}\mathbf{x}[p]\mathbf{x}^H[p], \tag{2.17}$$

where P is the number of temporal samples used in the estimate.

When the data vector, **x**, contains data samples which have been delayed in time as in (2.6), the steering vector, **a**, in (2.16), is simply a vector of ones. This is because the receiver has already been steered such that the signal of interest appears to be arriving from broadside. The estimated covariance matrix based on delayed data samples is sometimes referred to as the *steered covariance matrix*. In a narrowband scenario, implementing the steering as phase shifts in the steering vector is equivalent to steering using a time delay. In the broadband case, a time delay gives more accurate results.

Estimating the covariance matrix

The sample covariance matrix given in (2.17) is often not sufficiently robust in an active transmission environment, for several reasons. First, (2.17) requires a large number of temporal samples to obtain a reliable estimate of $\hat{\mathbf{R}}$. In [17, Chapter 7.3], $P > 2M$ is recommended. This is not always possible because of the non-stationarity of the received signals. Second, in an active transmission system the assumption that the signal is uncorrelated from the noise and interference is violated, causing *signal cancellation*. Since most of the energy backscattered toward the receiver consists of echoes from the same transmitted pulse, there is in general significant coherency between the received echoes. The result of signal cancellation is potentially severe underestimation of the signal amplitudes [21], [8, chapter 7.3.4].

Subarray averaging effectively decorrelates the signal component from the noise-and-interference component, such that signal cancellation effects are reduced or mitigated [8, chapter 7.3.4], [22]. The process involves dividing the receiver array into smaller, overlapping segments of L elements each, estimating the spatial covariance matrix for each subarray and using the average covariance matrix estimate in (2.16). Dividing the receiver array into subarrays is illustrated in Figure 2.9. A robust estimate of $\mathbf{R}$ combines the sample covariance matrix with spatial smoothing. The estimated covariance matrix using K subarrays and P temporal samples can be expressed as

$$\hat{\mathbf{R}}[n] = \frac{1}{P \times K} \sum_{p=-(P-1)/2}^{P/2} \sum_{k=0}^{K-1} \mathbf{x}_k[n-p]\mathbf{x}_k^H[n-p], \tag{2.18}$$

where $\mathbf{x}_k$ contains the delayed measurements from the sensors in subarray k, and the superscript H denotes the conjugate transpose operation. The MVDR amplitude estimate is found by applying the optimal weights from (2.16) to the delayed data from each of the K subarrays and averaging over the number of subarrays.

Diagonal loading can be applied for additional robustness [23], [24]. Diagonal loading implies adding a small value, ϵ, to the diagonal of the covariance matrix estimate, such that $\hat{\mathbf{R}}[n]$ is replaced by $\hat{\mathbf{R}}[n] + \epsilon\mathbf{I}$. Diagonal loading is analogous to adding spatially white noise to the data, and has the effect of widening the mainlobe of the steered response.

2.4.3 The adaptive APES beamformer

The amplitude and phase estimation (APES) beamformer is an implementation of the optimal MVDR beamformer. The solution to the APES beamformer is found by replacing $\mathbf{Q}$ by its estimate, $\hat{\mathbf{Q}}$, in (2.13) and solving the minimization problem. The solution is

$$\mathbf{w}_{\text{APES}} = \frac{\hat{\mathbf{Q}}^{-1}\mathbf{a}}{\mathbf{a}^H\hat{\mathbf{Q}}^{-1}\mathbf{a}}. \tag{2.19}$$

The noise covariance matrix, $\mathbf{Q}$, can be estimated as [25]

$$\hat{\mathbf{Q}} = \hat{\mathbf{R}} - \mathbf{g}(\mathbf{k})\mathbf{g}^H(\mathbf{k}), \tag{2.20}$$

where $\mathbf{g}(\mathbf{k})$ contains an estimate of the desired signal arriving from the steering direction:

$$\mathbf{g}(\mathbf{k}) = \frac{1}{K}\sum_{k=0}^{K-1} \mathbf{x}_k e^{-j\mathbf{k}^T\mathbf{p}_k}, \tag{2.21}$$

K is the number of subarrays, and $\mathbf{x}_k$ is the data vector received by subarray k. The subscript k is not to be confused with the wavenumber vector, $\mathbf{k}$.

The adaptive MVDR beamformer is often chosen because it requires knowledge of the data covariance matrix, but not of the noise covariance matrix. In general, the former is known (because it is measured), while the latter can be tricky to estimate. The APES beamformer has an advantage when it comes to robustness, since it does not include the signal of interest in the minimization problem, and therefore cannot accidentally suppress it.

2.4.4 The low complexity adaptive (LCA) beamformer

The LCA beamformer was proposed in 2009 in the context of medical ultrasound imaging [26]. It is based on the same optimization criterion as the adaptive MVDR beamformer, but the solution space is reduced yielding far lower computational complexity and increased robustness. Instead of allowing full adaptability, the LCA chooses between a finite set of P pre-defined window functions. The LCA beamformer chooses the window that minimizes the cost function:

$$\min_{p} E\left\{|\mathbf{w}_p^H \mathbf{x}|^2\right\}, p = \{0, 1, ...P - 1\} \tag{2.22}$$

for each image pixel. In practice, $E\left\{|\mathbf{w}_p^H \mathbf{x}|^2\right\}$ can be estimated by $|\mathbf{w}_p^H \mathbf{x}|^2$ [26].

The LCA has several advantages compared to the fully adaptive MVDR and APES beamformers. First, since the solution space is reduced, the computational burden is significantly reduced. Second, it is more robust than the fully adaptive methods. This inherent robustness makes diagonal loading and subarray averaging unnecessary.

The pre-defined window functions can be chosen freely, but in most cases common window functions such as those in Figure 2.6 represent a good choice. Including *steered* windows, or windows with peaks not at broadside but slightly off to either side, is recommended [26]. When looking at the weights chosen by the MVDR and APES beamformers, they are often chosen such that the beam is steered in order to avoid regions of noise or interference.

2.4.5 Adaptive methods based on aperture coherence

The coherence factor (CF) and its relative, the scaled Wiener postfilter (SWiP), are adaptive imaging methods which are fundamentally different to the adaptive MVDR and APES beamformers. The coherence-based methods are intuitively appealing, simple to implement, and their computational burden is relatively small. The main idea behind the coherence-based methods is that when steering the receiver towards a point of interest, the aperture coherence, defined as the ratio of the coherent energy to the incoherent energy received by the array, gives an indication of the quality of the received signal. A highly directive wavefield without noise results in a high aperture coherence. If, on the other hand, the wavefield has been distorted by e.g. noise or multipath propagation, the signals measured by the different receivers are less similar, i.e., the aperture coherence drops [27], [28], [29].

The CF was proposed as a means of quantifying the quality of each image pixel in a medical ultrasound image [30]. Later, it was extended to an imaging method by combining the CF with a conventional DAS beamformer [31]. Recently, the CF method was interpreted in the context of Wiener filtering and Wiener postfiltering [19]. It was shown that the CF method could be interpreted as a statistically optimal Wiener postfilter applied to the output from a conventional beamformer, but that the amount of noise was over-estimated. This observation explained the undesired behaviour of the CF method when applied to low-SNR scenarios, where it tends to introduce image artifacts. The SWiP was proposed as an alternative, and allows for a smooth transition from the effective but harsh CF method to the robust Wiener postfilter [19]. The SWiP and CF methods are not referred to as beamformers in this thesis, but as *adaptive imaging methods*.

The coherence factor (CF)

The CF is based directly on the aperture coherence. It is sometimes referred to as the *Mallart-Fink focusing factor* [32], and in seismics it is referred to as *semblance* and used to aid the seismic velocity picking process [33]. The CF is defined as the ratio of the coherent sum to the incoherent sum over an M-element array [30]:

$$\mathrm{CF} = \frac{|\sum_{m=0}^{M-1} x_m[n]|^2}{M\sum_{m=0}^{M-1} |x_m[n]|^2}. \tag{2.23}$$

The CF is a number between 0 and 1, quantifying the aperture coherence. The CF method uses the CF weights of (2.23) as a scaling factor by which the output from a conventional DAS beamformer is multiplied. In this way pixels with a low CF value are considered unreliable and therefore suppressed, while pixels exhibiting a high CF value are preserved. The CF method has strong noise suppression capabilities, but fails in low-SNR scenarios and speckle scenes because it over-compensates for the noise [19].

The scaled Wiener postfilter (SWiP)

The SWiP was introduced in the context of medical ultrasound imaging as a robust alternative to the CF. It is derived in [19] using Wiener filter theory. The SWiP contains a user-defined parameter, α, which allows a sliding transition from the rather aggressive CF method to the robust Wiener postfilter. The flexibility of the SWiP makes it a promising candidate in a range of sonar imaging applications.

For each image pixel, the SWiP weights are computed as

$$H_{\mathrm{SWiP}} = \frac{|A|^2}{|A|^2 + \alpha \mathbf{w}^H \mathbf{Q} \mathbf{w}}, \tag{2.24}$$

where A is the amplitude of the desired signal, **w** contains the beamformer weights of the DAS beamformer, and **Q** is the noise covariance matrix. In practice, A and **Q** are unknown and need to be estimated [19]. For comparison, the CF weights from 2.23 can be re-written as

$$H_{\mathrm{CF}} = \mathrm{CF} = \frac{|A|^2}{|A|^2 + M \mathbf{w}^H \mathbf{Q} \mathbf{w}}. \tag{2.25}$$

The CF and the SWiP add little computational complexity compared to the DAS beamformer. The weights are computed using the aperture coherence after delay but before summing the sensor measurements. The weights matrix, which has the same dimensions as the output image after beamforming, is simply multiplied pixel by pixel with the beamformed image. Thus the original DAS image can be kept in addition to the SWiP- or CF-weighted image.

Adaptive beamformers applied to curved arrays

In applications such as fish-finding sonars and navigation, linear arrays are not suitable because of the need for a 360 degree field of view. Often, cylindrical or spherical arrays are used instead. Several array processing techniques, including sub-array averaging, were developed for uniformly

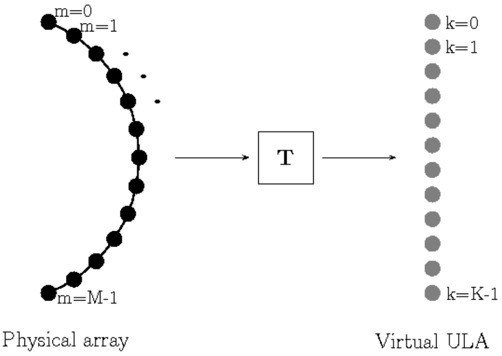

Figure 2.10: An interpolated array transformation maps the data from a physical curved array to a virtual ULA.

sampled, linear arrays (ULAs) and cannot be applied directly without a loss in performance, since the steering vector does not display the desired Vandermonde structure [34], [35]. *Interpolated array transformations* were developed to take the data received by a physical array and transform it to a virtual array displaying a structure suitable for processing techniques such as sub-array averaging. The concept of an interpolated array transformation is illustrated by Figure 2.10. The virtual array is usually chosen to be a ULA, but in general it can be of any desirable configuration.

The most common interpolated array transformation is probably the one proposed by Friedlander [36]. The goal of the Friedlander transformation is to find a transformation matrix, $\mathbf{T}$, mapping the received data vector, $\mathbf{x}$, to a virtual array displaying the desired structure. The data vector for the virtual array, $\mathbf{y}$, is computed as

$$\mathbf{y} = \mathbf{T}\mathbf{x}. \tag{2.26}$$

The transformation matrix, $\mathbf{T}$, can be computed offline and therefore the transformation implies a modest increase in computational burden.

2.4.6 Robustness of adaptive beamformers

A major concern when applying adaptive beamforming methods to operational systems is their robustness in a practical setting. The performance of adaptive beamforming methods can be severely degraded when there are discrepancies between the assumed model and the actual scenario. The adaptive MVDR beamformer is particularly sensitive, since the objective function is to minimize the power of the beamformer output, under the constraint of unit gain in the steering direction. The only mechanism stopping the MVDR beamformer from trying to force the output to zero is the distortionless response constraint. In the case of inaccuracies in the model, its performance degrades rapidly unless measures are taken. The APES beamformer is more robust, since the signal of interest is not present in the minimization problem. The adaptive MVDR beamformer is sensitive to:

- errors in the sensor positions,
- defective sensors,
- errors in the assumed speed of propagation,
- errors in the steering direction, and
- coherence between the signal of interest and noise or interfering signals.

Several techniques have been developed to reduce the sensitivity to such errors. Diagonal loading, as described in chapter 2.4.2, involves adding a small value to the diagonal of the estimate of the covariance matrix. As a result, the beamformer response is widened, making it less sensitive to errors in the model parameters. At the same time, the obtainable image resolution is reduced. As the choice of ϵ increases, the performance of the adaptive beamformer approaches that of the conventional DAS. Diagonal loading also ensures that the estimated covariance matrix is invertible.

The adaptive MVDR and APES beamformers both assume that the signal is uncorrelated with the noise and interference. When this assumption does not hold, subarray averaging is recommended in order to decorrelate the signal from the noise and interference. The main reason for applying subarray averaging in an active transmission environment is to reduce the coherency between the signal of interest and interfering signals, and to obtain a more robust estimate of the covariance matrix. A secondary effect is that the response is widened as with diagonal loading, making the beamformer generally more robust.

Another way to add robustness to adaptive beamformers is to add additional constraints [17, chapter 6]. All of the abovementioned techniques have in common that they remove some of the adaptivity of the beamformer, thereby compromising the obtainable image resolution and noise-suppression capabilities, in order to add robustness.

The LCA is inherently robust and does not require any of these techniques. It is affected by errors in model parameters in the sense that if the steering direction is wrong, the distortionless constraint ensures unit gain in the wrong direction while it chooses the window that minimizes the output power. However, because it is limited to using one of the pre-defined windows, the worst case scenario is that it chooses a window that is sub-optimal. Choosing reasonable window functions and limiting the steering of the receive beam to for instance a fraction of the beamwidth, is a sufficient measure to ensure robustness.

The coherence-based CF and SWiP methods are also inherently relatively robust with respect to errors in the model parameters. Perturbations in element positions or errors in the steering direction will cause the aperture coherence to drop, and as a result the output will be attenuated more than necessary. However, there is no minimization problem trying to force the output to zero. Therefore, the performance is not expected to degrade dramatically as it can do for the MVDR beamformer unless proper measures are taken.

2.5 Performance metrics

How do we determine what is a good image and what is not? One way is to qualitatively assess the images simply by looking at them. The human eyes and brain are extraordinarily well equipped for recognizing complex patterns which a computer may struggle to find. In many cases the end user of the image *is* a human. In other cases, the image may be passed on to a machine that uses some algorithm to perform target recognition or biomass estimation. Quantitative measures can reveal differences which are missed when subjectively evaluating the image quality. Defining quantitative performance metrics that apply to different applications is non-trivial. Some possible performance metrics are suggested below.

- **Qualitative assessment:** Looking at the images and assessing whether they are clear or blurry, if details are clear or difficult to recognize, if they appear contaminated by noise, and so on.
- **Contrast ratio (CR):** The contrast ratio (CR) between a shadow region and a background or highlight region can be used to quantify how well noise is suppressed. CRs in other regions where the true CR is known, can be used to determine how well amplitudes are preserved.
- **Speckle statistics:** Many scatterers within a resolution cell give rise to a speckle pattern. Statistical descriptions of fully developed speckle exist, and can be used to quantify how an adaptive method affects these regions.
- **Characteristics of the steered response:** For conventional, non-adaptive beamforming methods, the steered response obtained when imaging a single or a few point sources can be used as a performance metric. The -3 dB mainlobe width can be measured and used to define the resolution capabilities and the sidelobe levels and location of the nulls give information about the noise suppression capabilities and interference rejection abilities. For adaptive methods these measurements should be used as an indicator only, since they are situation-dependent as explained below.
- **Image resolution:** There are several possible definitions of resolution. A common definition is the minimal separation at which two sources can be separated by some value, for instance 3 dB.

  Care has to be taken when using characteristics of the beampattern and the image resolution to evaluate the performance of adaptive beamformers, since the performance is *situation dependent*. For a conventional beamformer, the weights are pre-defined and the beampattern determined once and for all. The mainlobe has a certain width and the height of the sidelobes and positions of the nulls are known, and are independent of the scene. In adaptive beamforming methods this is not the case. The weights are chosen dynamically depending on the data measurements, and thus the beampattern is highly dependent on the situation. Thus it is not possible to extrapolate from for example the case of two reflectors to a general case. The measured mainlobe width, resolution or sidelobe levels in one scenario gives an *indication* of the general performance of the method, but one should be careful about extrapolating these results to a different scene.

- **Sensitivity:** The ability to detect a weak target, or a target with low intensity.
- **Dynamic range:** The ability to detect a low-intensity target in the presence of a high-intensity target.
- **Spatial and temporal coherence:** The degree of coherence between two signals can be related to the system SNR, and as such can be a meaningful performance metric. Intuitively this is similar to the motivation behind the aperture-based adaptive imaging methods discussed in chapter 2.4.5. If the signal can be assumed static either in time (e.g. from one ping to the next) or in space (e.g. between two sensors), while undesired noise and interference is not, the coherence should increase if the noise and interference is suppressed.

  Assume two signals, s_1 and s_2, displaced either in time or in space and sampled at time instant t. The *complex degree of coherence* is described by the normalized mutual coherence function [37, pp 499-503], [11, p 96]

  $$\gamma_{12}(\tau) = \frac{E\left\{s_1(t)s_2^*(t+\tau)\right\}}{\left[E\left\{|s_1|^2\right\}E\left\{|s_2|^2\right\}\right]^{1/2}}, \tag{2.27}$$

  where τ is the time delay between s_1 and s_2. The maximum value of the mutual coherence function is often used to define the coherence [11]

  $$|\gamma| = \max_{\tau} |\gamma_{12}(\tau)|. \tag{2.28}$$

  Assuming a Gaussian distribution of signal and noise, the SNR can be derived from the coherence [11]:

  $$\mathrm{SNR} = \frac{|\gamma|}{1-|\gamma|}. \tag{2.29}$$

Chapter 3

Summary of publications

3.1 Paper I

A. E. A. Blomberg, I. K. Holfort, A. Austeng, J. -F. Synnevåg, S. Holm and J. A. Jensen, "APES beamforming applied to medical ultrasound imaging", *Proc. IEEE Ultrasonics symposium*, Rome, 2008.

Paper I considers and compares the adaptive MVDR and APES beamformers when applied to simulated medical ultrasound data. The simulations are based on Field II, using a 92-element uniformly sampled, linear receiver array with $\lambda/2$ spacing. We show that while the MVDR beamformer offers superior resolution capabilities, it is not as robust as the APES beamformer. In particular, the MVDR is affected by signal cancellation causing under-estimation of the signal amplitudes unless sufficient subarray averaging is used, and when imaging a cyst in speckle it has an undesirable effect on the speckle pattern unless temporal averaging is applied.

When varying the subarray length, L, from $M/4$ to $M/2$, the APES beamformer displays near-constant behaviour in terms of mainlobe width of the steered response and the ability to separate two sources. Also, it shows reliable and consistent amplitude estimates for all choices of L. The MVDR beamformer, on the other hand, is more sensitive to the choice of L and requires $L= M/4$ to avoid under-estimating the signal amplitudes. When compared to the conventional DAS beamformer, both adaptive methods offer improved image quality in terms of increased resolution and noise suppression capabilities.

3.2 Paper II

A. E. A. Blomberg, A. Austeng and R. E. Hansen, "Adaptive beamforming applied to a cylindrical sonar array using an interpolated array transformation", *IEEE Journal of Oceanic Engineering*. Accepted for publication Sep. 14, 2011.

Paper II considers the use of adaptive beamforming applied to a cylindrical fish finding sonar array. While subarray averaging is required to obtain a robust estimate of the covariance matrix and to avoid signal cancellation, the non-linear shape of the receiver array makes this processing step non-trivial. The subarray averaging technique requires the steering vector of the receiver array to display a so-called Vandermonde structure, which is not the case for cylindrical arrays.

We propose the use of an interpolated array transformation in order to map the data from the cylindrical receiver array onto a virtual ULA prior to adaptive beamforming.

We use a simulated environment developed at the Norwegian Defence Research Establishment (FFI) to illustrate the importance of applying such a transformation. Results from simulations as well as experimental data are in agreement with the findings from Paper I. Using experimental data from the Simrad SX90 sonar, we show that when performing an interpolated array transformation prior to beamforming, the adaptive APES and MVDR beamformers offer a significant improvement in azimuth resolution compared to the DAS beamformer. When imaging a corner reflector in the water column, the azimuth resolution, defined here as the 3dB width of the mainlobe of the steered response, is increased by 40-50 % by the MVDR beamformer and 20-30 % by the APES beamformer.

3.3 Paper III

A. E. A. Blomberg, A. Austeng, R. E. Hansen and S. A. V. Synnes, "Improving sonar performance in shallow water using adaptive beamforming", *IEEE Journal of Oceanic Engineering*. Revised version submitted Aug. 30, 2011.

This paper considers the use of adaptive beamforming for improved sonar performance in shallow waters, where multipath propagation often is the limiting factor. Multipath signals, i.e., signals which have taken a different path than the direct return from the seafloor to the receiver, interfere with the desired direct return and cause the SNR to drop.

We investigate the use of adaptive beamforming to suppress interfering multipaths, hence improving the sonar performance and potentially increasing the sonar range. We base our study on experimental data provided by NATO Undersea Research Center (NURC). The data was collected near La Spezia, Italy, in a shallow water region where the water depth is about 20 m. In our study we focus on the use of a small receiver array suitable for mounting on a towed platform such as an autonomous underwater vehicle (AUV). We measure the performance using the ping-to-ping coherence of the time series recorded by the receiver array. To gain an understanding of how multipath propagation affects the data from this experiment, we model which multipath signals interfere with the direct return, and the relative magnitude of each.

We found that the improvements achieved by the use of adaptive beamforming is highly dependent on the direction of arrival (DOA) of the interfering multipath signals. When the DOA of the multipath is well separable from that of the direct return, a modest but consistent improvement was observed. We also found that the improvements offered by adaptive beamforming are attributed to the adaptive beamformers' ability to steer the mainlobe of the receiver to avoid the dominating multipath. The gain obtained by placing a null in the direction of an interfering signal which would appear in one of the sidelobes of a conventional beamformer, is marginal. For this reason, adaptive methods only offered an improvement when the receive beam was wide enough to cover the direct return and one or more multipath signals. We propose the use of the LCA beamformer which outperforms the MVDR beamformer since it does not require subarray averaging, and thus can utilize the full extent of the array. We also found that when using conventional beamformers, uniform weighting was preferable since there was more to gain by having a narrow mainlobe than low sidelobe levels.

3.4 Paper IV

A. E. A. Blomberg, R. E. Hansen, S. A. V. Synnes and A. Austeng, “Improved interferometric sonar performance in shallow water using adaptive beamforming”, *Proceedings of underwater acoustic measurements (UAM)*, Kos, Greece, June 2011.

This paper is inspired by the results from Paper III. The results from Paper III indicate that for small receiver arrays, the LCA beamformer is able to suppress interfering multipath signals to a certain degree, hence improving the SNR. In this paper we investigate the use of the LCA for improved interferometric imaging. Using two small receiver arrays consisting of two or three elements each, configured as an interferometer, we investigate the potential gain of using LCA beamforming separately on each receiver array, prior to computing the interferogram.

The error in the height estimate from the interferogram is directly related to the spatial coherence between the two receiver arrays. As multipath signals begin to interfere with the direct return, the spatial coherence decreases and the SNR along with it. Often, the maximum range of an interferometric sonar is defined as the point where the spatial coherence drops below a certain value. Using the same experimental data as in Paper III, we show that the spatial coherence and thus the useful imaging range can be improved by using LCA beamforming on the receiver side.

3.5 Paper V

A. E. A. Blomberg, C.-I. C. Nilsen, A. Austeng and R. E. Hansen, "Adaptive sonar imaging using aperture coherence", *IEEE Journal Of oceanic Engineering.* Submitted Oct. 1, 2011.

In this paper we introduce the SWiP as an adaptive imaging method for sonar imaging. Using simulations and experimental data, we investigate the performance of the SWiP and compare it to the CF method and to the conventional DAS beamformer. While the CF method images point targets very well and has superior noise suppression capabilities, it also introduces image artifacts in speckle scenes. The SWiP with a reasonable choice of the parameter α, improves the image quality by attenuating noisy samples, while preserving the speckle pattern.

We use experimental data from two different applications; a fish finding sonar imaging an object in the water column, and a sidescan sonar imaging the wreck of an oil tanker resting on the seafloor. Using data from the Simrad SX90 fish finding sonar, we show that the SWiP significantly improves the image quality by suppressing sidelobe energy and background noise. The sidescan data represents a more challenging scenario, because of the incoherent speckle pattern originating from the many random scatterers on the seafloor. In this case, the CF method introduces image artifacts; the region surrounding the wreck is suppressed giving the appearance of empty space where there is actually a sandy seafloor. The SWiP performs well, reducing noise such that details in the image such as the masts on the ship appear more clearly defined.

The main contribution of this paper is to introduce the SWiP as a promising method for sonar imaging. It is fundamentally different to the other adaptive methods discussed in Papers I-IV, as it does not ensure a distortionless response in the direction of interest, and it does not manipulate the beampattern in order to suppress noise and interfering signals. However, it attenuates pixels which are perceived as noisy while preserving noise-free pixels. It results in pleasing images, which appear less noisy than the output from a conventional beamformer.

Chapter 4

Summary and Discussion

This Chapter summarizes the main contributions of this thesis, and offers a short discussion on some points that either could have been done differently or that need to be clarified. Finally, a case study is presented, comparing the different adaptive methods from papers I to V and highlighting their differences.

The main contributions of this thesis to the field of adaptive sonar imaging are:

- An analysis of the adaptive MVDR and APES beamformers with respect to their resolution capabilities, and their robustness in terms of correctly estimating the amplitude of a desired signal (Paper I).
- A discussion on the use of adaptive beamforming applied to curved arrays (Paper II).
- The description and validation of an interpolated array transformation in order to apply adaptive beamforming to a cylindrical sonar array (Paper II).
- Analysis of the performance of the adaptive APES and MVDR beamformers when applied to a fish finding sonar, and validation of the methods using experimental sonar data (Paper II).
- A study on the effects of multipath propagation in shallow water regions, including the use of conventional and adaptive beamforming methods for improved sonar performance (Paper III).
- A comparison of the performance of conventional and adaptive beamforming methods used for interferometric imaging in shallow waters (Paper IV).
- Introduction of two coherence-based adaptive methods for improved sonar imaging (Paper V).

Although the main topic of this thesis is adaptive beamfoming for sonar imaging, Paper I considers adaptive beamforming applied to medical ultrasound imaging. The results are still applicable to sonar imaging, because of the physical and conceptual similarities between medical ultrasound imaging and sonar imaging. The basic challenge is the same - to correctly estimate the reflectivity of each point in the scene, yielding a high-resolution image without noise and artifacts.

In papers I and II, the use of the term *resolution* could have been more precise. Several alternative definitions of the term exist. A common definition is the minimum distance for which two points can be separated by 3 dB. In order to state that one method has better resolution than another, the points need to be too closely spaced to be resolved by one method, while another is able to resolve them. In paper I we state that the adaptive MVDR and APES beamformers offer improvements in resolution when imaging two closely spaced point scatterers. However, the point scatterers are not too close to be resolved using a conventional beamformer. In hindsight, the points should either have been placed closer together, or the statement of improved resolution should have been clarified. The results give a clear indication that the resolution is in fact improved through adaptive beamforming, but based on the definition above the examples are not sufficient to prove this.

In paper II, we use the term resolution when evaluating the results from experimental data imaging a single reflector. Although the width of the steered response gives an indication of the resolution capabilities of the method, as discussed in chapter 2.5, it is not strictly speaking correct to extrapolate and conclude that the resolution in a general case is improved. Finding a good way to quantitatively assess the performance of adaptive methods is non-trivial, as discussed in chapter 2.5.

Papers III and IV consider sonar imaging in shallow water regions, where multipath propagation constitutes a major challenge. The results and conclusions we make are based on data from an experiment carried out in a shallow water region in Italy. Further studies using simulations would be beneficial in order to verify our findings in a controlled setting.

The adaptive CF and SWiP methods presented in paper V are both used in conjunction with a conventional DAS beamformer. They could, however, both be implemented as a postfilter after any distortionless beamformer, including the adaptive MVDR, APES, and LCA beamformers. In this way the high resolution capabilities of the adaptive beamformers could be combined with the superior noise suppression capabilities of the coherence-based methods. Combining the CF method with the MVDR beamformer has been proposed in the context of medical ultrasound imaging [38].

Case study

In papers I through V, different adaptive methods have been applied in a number of settings ranging from simple simulated scenes to complex speckle scenes, and experimental data from a fish finding sonar, a sidescan sonar, and a vertically oriented sonar array operating in a shallow water region. For completeness, a case study is included here, comparing the performance of the different methods when applied to the same data. The aim is to highlight the properties of and differences between the different methods. The comparison includes the uniformly weighted and Hanning-weighted DAS beamformers, the adaptive MVDR and APES beamformers, the LCA beamformer, the CF, and the SWiP. The CF images are not included here since we concluded in Paper V that the CF is not well suited for imaging speckle scenes, because of its tendency to introduce image artifacts. Quantitative CR measurements are included for all methods, including the CF, in Table I.

This study is based on two data sets; simulated multibeam sidescan data from a complex speckle scene, and sidescan sonar data from the Kongsberg Maritime HISAS 1030 sonar operated in real-aperture mode. The simulation setup and the HISAS 1030 sonar are both described in Paper V. In this study, the simulated scene has been cropped to include only one cylinder, and an additional point scatterer has been added (compared to the scene in Paper V).

Figure 4.1 shows images of the simulated scene containing a vertically oriented cylinder and two strong point scatterers, created using each of the beamforming and imaging methods. The area containing the two point scatterers is indicated by the rectangle in Figure 4.1(a), and enlarged in Figure 4.2. Figure 4.3 shows images of the wreck of the oil tanker “Holmengrå”, obtained using experimental data from the HISAS 1030 sidescan sonar. The wreck is about 68 m long and 9 m wide, and rests on the seafloor at a depth of 77 m. Table I summarizes the speckle/shadow CR for each method, for the simulated scene and for the experimental scene. The CR is measured as the ratio of the mean intensity level in a speckle region of the image, to the mean intensity level inside the shadow region. In an ideal case of complete noise suppression this value should reach infinity.

The parameters used when implementing the different methods are as follows: In all cases a 32-element receiver was used. The MVDR and APES beamformers were both implemented using a sub-array length of L=16 elements, and 3 % diagonal loading. For the LCA beamformer, 18 pre-defined windows were used. The windows were based on rectangular and Hanning windows, steered to 0, $\pm 1/4$ BW, $\pm 1/8$ BW, $\pm 1/16$ BW, and $\pm 1/32$ BW, where BW denotes the two-sided -3 dB beamwidth of a 32-element uniformly weighted DAS beamformer. For the SWiP, $\alpha = M/8$ was used. The CF is parameter-free.

	DAS	DAS Hanning	MVDR	APES	LCA	SWiP α=M/8	CF	Desired value
CR simulation	13.8	20.8	19.0	20.9	19.2	25.9	37.2	∞
CR wreck	11.9	19.9	18.4	19.4	18.6	23.5	42.7	∞

Table I: CR measurements in dB for each imaging method.

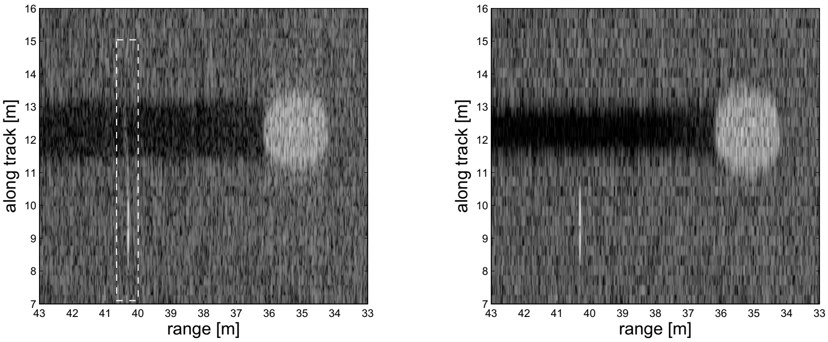

(a) uniformly weighted DAS

(b) Hanning-weighted DAS

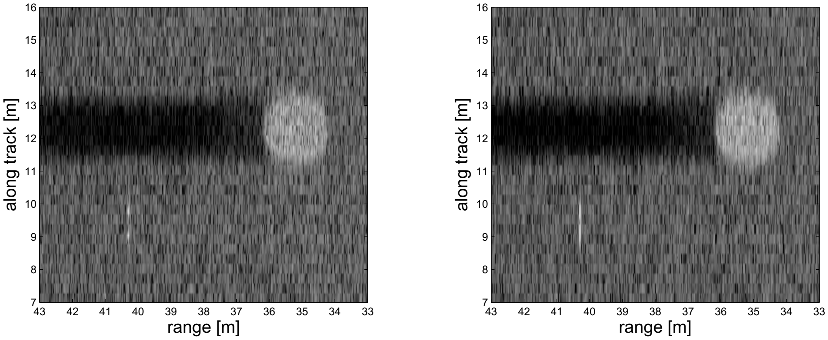

(c) MVDR

(d) APES

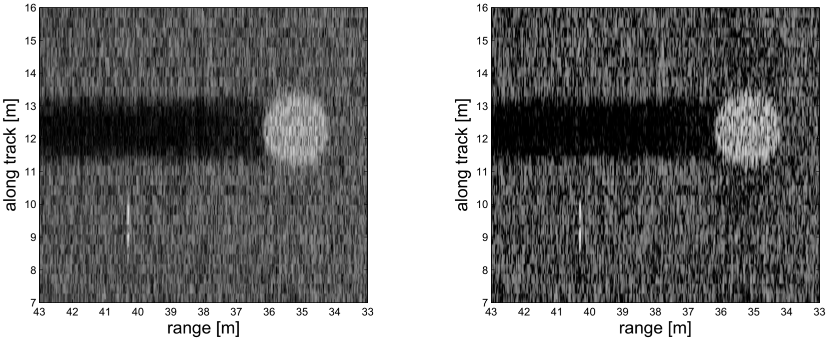

(e) LCA

(f) SWiP

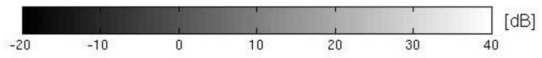

Figure 4.1: A simulated scene consisting of a cylinder in speckle and two point scatterers, imaged using each of the adaptive imaging methods discussed in Papers I-V. The white rectangle in (a) indicates the location of the point scatterers, and is enlarged in Figure 4.2. Each image has been normalized by its mean speckle level.

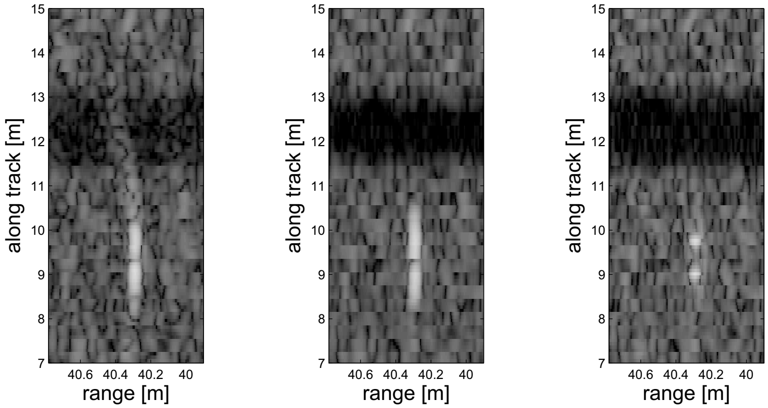

(a) uniformly weighted DAS

(b) Hanning-weighted DAS

(c) MVDR

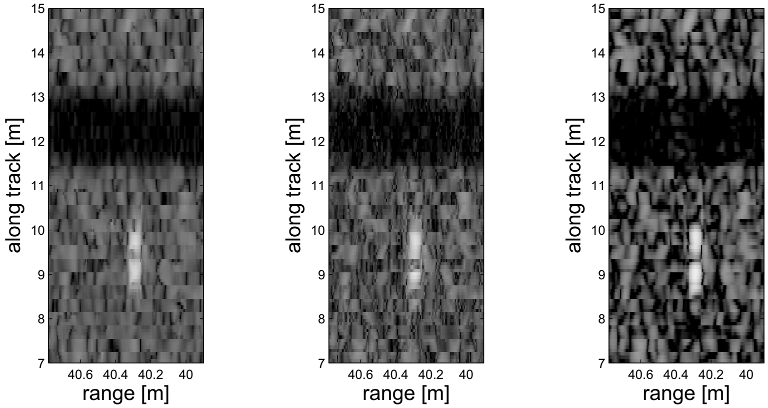

(d) APES

(e) LCA

(f) SWiP

Figure 4.2: Enlargement of the area in the simulated scene containing the two point scatterers.

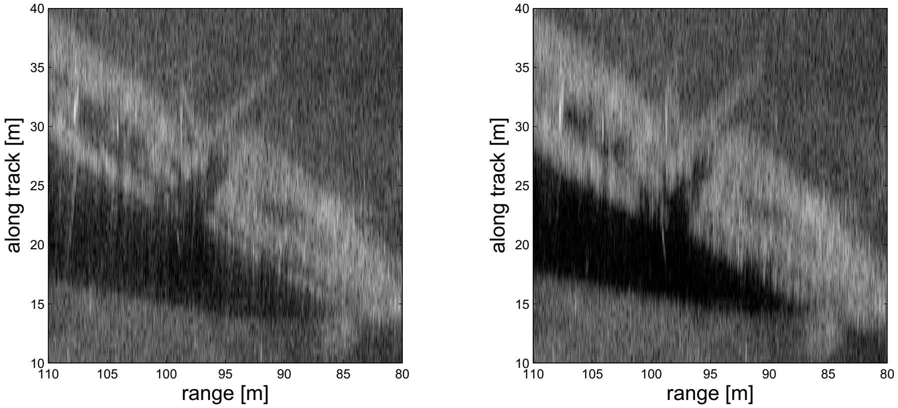

(a) uniformly weighted DAS

(b) Hanning-weighted DAS

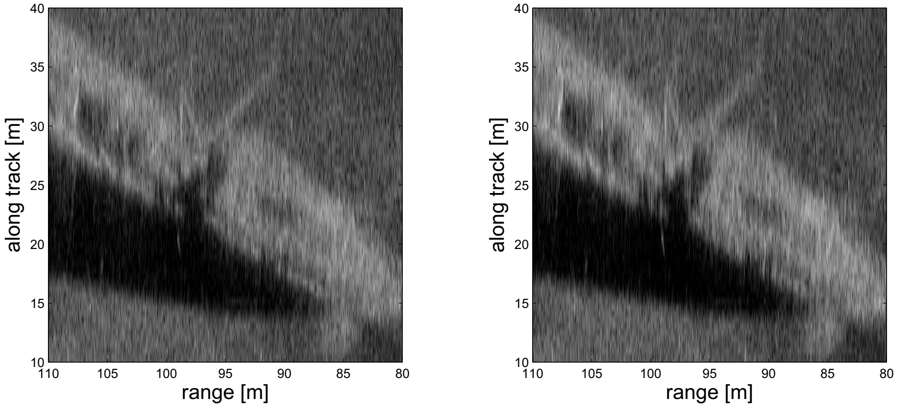

(c) MVDR

(d) APES

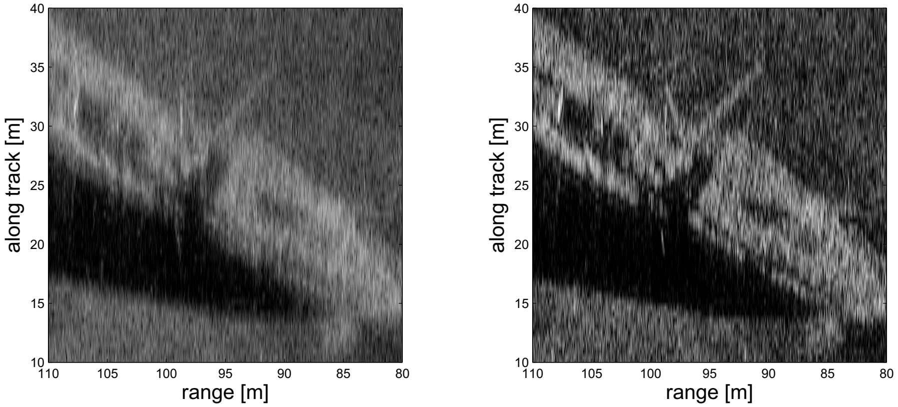

(e) LCA

(f) SWiP

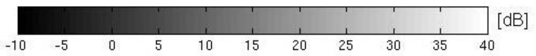

Figure 4.3: Sidescan image of the shipwreck "Holmengrå", imaged using each of the adaptive imaging methods discussed in Papers I-V. Each image is normalized by its mean speckle level.

The results from the case study can be summarized as follows:

- **The unweighted DAS beamformer** is simple and robust, and has better resolution capabilities than the Hanning-weighted DAS beamformer, but limited noise-and-interference suppression capabilities. Its -13 dB sidelobes causes the images in Figures 4.1 and 4.3 to appear noisy. This is particularly visible in the shadow regions where noise and sidelobes from strong scatterers can be seen. The speckle/shadow CR is poor compared to the other methods.

- **The Hanning-weighted DAS beamformer** is simple and robust, and offers improved noise-and-interference suppression capabilities at the cost of reduced image resolution. The effect is clear in Figure 4.1 where the shadow region contains little (visible) noise, but appears narrower than it is because of the wide mainlobe of the Hanning-weighted DAS beamformer. The CR values are higher than those of the uniformly weighted DAS, verifying its superior noise suppression capabilities.

- **The adaptive MVDR beamformer** offers good noise-and-interference suppression capabilities as well as superior resolution capabilities. The CR values for the simulated and the experimental scene are 19.0 dB and 18.4 dB, respectively. This is close to that of the Hanning-weighted beamformer. The two point scatterers in Figures 4.1 and 4.2 appear as two small, clearly separated points, indicating the high resolution capabilities of the MVDR beamformer. This is confirmed in the experimental data example in Figure 4.3.

- **The adaptive APES beamformer** displays slightly better noise suppression capabilities than the MVDR beamformer, quantified by slightly higher CR values. The resolution capabilities are somewhat lower than the MVDR beamformer. Previous work concludes that the APES beamformer offers lower resolution than the adaptive MVDR beamformer in general. In turn, the APES beamformer is more robust to errors in the model parameters, and it offers reliable amplitude estimates in the direction of interest. It can, however, introduce “false peaks” in other directions. The APES beamformer is excellent at estimating the amplitude of a signal of interest when the direction is known [39].

- **The adaptive LCA beamformer** offers much of the same advantages as the fully adaptive MVDR and APES beamformers, but it is less computationally demanding and does not require the same robustification methods as its fully adaptive counterparts. The CR values of 19.2 and 18.6 are slightly lower than the values for the Hanning-weighted DAS beamformer, but well above those of the uniformly weighted DAS beamformer. The resolvability of the two point scatterers in Figure 4.2 and the details visible in Figure 4.3 indicate that its resolution capabilities in these examples is between that of the uniformly weighted DAS and the MVDR beamformers. The pre-defined windows used in this example are not optimized for imaging quality.

- **The CF method** is excellent at enhancing point scatterers in the presence of incoherent noise. It outperforms the other methods in terms of speckle/shadow CR. However, the CF is not suited for imaging speckle scenes when conservation of the speckle pattern is desired, and may introduce image artifacts as shown in Paper V.

- **The SWiP** is a robust version of the CF method that is well suited for imaging point scatterers as well as speckle scenes. With a suitable choice of α, it is able to attenuate pixels that are contaminated by noise or interference. The CR values of 25.9 and 23.5 show that it outperforms all other methods except the CF method in terms of suppressing noise and interference in the shadow region. Its resolution capabilities are limited by that of the uniformly weighted DAS beamformer, as illustrated by the point scatterers in Figure 4.2. In the same Figure, its ability to suppress the sidelobes from the point scatterer is seen. The result on a complex scene such as in Figure 4.3 is that the shadow region is enhanced and details appear more clearly defined because they are enhanced relative to the noisy surroundings.

Chapter 5

Future work

In this thesis, we have considered adaptive beamforming and coherence-based imaging methods for active sonar imaging. Key challenges such as coherent signals, non-linear arrays, robustness in a practical setting, and computational cost are addressed. There are, however, many interesting questions yet to be answered. Here, we list a few of the most relevant:

- **Tune adaptive methods to a specific application**
  In this thesis adaptive beamformers and adaptive coherence-based imaging methods have been applied to a range of sonar imaging applications. A possible next step is to take these adaptive methods one step further, adapting them to a specific application. The adaptive method could be targeted to for instance optimizing target classification, detecting gas bubbles in the water column, or enhancing shadow regions.

- **Extension to synthetic aperture sonar (SAS)**
  SAS has become a mature imaging method [5], and offers azimuth resolution beyond what we would normally expect from the adaptive beamforming methods discussed in this thesis. A natural extension of the work in this thesis is to investigate whether one can achieve even higher image quality by combining adaptive beamforming methods or coherence-based methods with SAS-processing.

- **Adding constraints for improved imaging in shallow water regions**
  The adaptive MVDR and APES beamformers have one constraint only - that the signal of interest is passed undistorted. When some knowledge exists about the environment and expected direction from which interfering signals arrive, there may be something to gain by adding additional constraints. In a multipath scenario, forcing a wide null in the expected direction of the first-order multipath from the sea-surface might be beneficial. This can be achieved by adding the constraint that the derivative of the response should be zero in the expected direction of the interference.

- **Further research on coherence-based adaptive imaging methods**
  In addition to imaging, coherence-based methods may be useful for other applications such as object classification, and for detecting and differentiating between moving targets and stationary objects in the water column.

- **Optimizing the choice of windows in the LCA**
  The LCA adaptive beamformer is used in Papers III and IV with a set of basic pre-defined

windows. The LCA shows promising results, and an interesting topic for further research is to optimize the choice of window functions for different applications. Issues to be addressed include how many windows are needed, and how much steering should be allowed.

Bibliography

[1] E. MacCurdy, *The Notebooks of Leonardo da Vinci.* Garden City, N.Y.: Garden City Publishing Co., Inc., 1942, ch. X.

[2] W. S. Burdic, *Underwater Acoustic System Analysis.* Prentice-Hall, 1984.

[3] X. Lurton, *An Introduction to Underwater Acoustics: Principles and Applications.* London, UK: Springer Praxis Publishing, 2002.

[4] R. Vaccaro, "The past, present, and future of underwater acoustic signal processing," *IEEE Signal Process. Mag.*, vol. 15, no. 4, pp. 21 –51, Jul. 1998.

[5] R. E. Hansen, *Introduction to Synthetic Aperture Sonar, Sonar Systems.* Available from: http://www.intechopen.com/articles/show/title/introduction-to-synthetic-aperture-sonar: InTech, N. Z. Kolev (Ed.), 2011.

[6] G. Franceschetti and R. Lanari, *Synthetic Aperture Radar Processing.* Boca Raton, FL, USA: CRC Press, 1999.

[7] R. O. Nielsen, *Sonar Signal Processing.* Artech House, 1991.

[8] D. H. Johnson and D. E. Dudgeon, *Array signal processing: Concepts and Techniques.* Englewood Cliffs, NJ, USA: Prentice Hall, 1993.

[9] P. Blondel, *The Handbook of Sidescan Sonar.* Geophysical Sciences, Springer Praxis Books, 2009.

[10] J. P. Fish and H. A. Carr, *Sound reflections: Advanced Applications of Side Scan Sonar.* LowerCape Publishing, 2001.

[11] R. F. Hanssen, *Radar Interferometry: Data Interpretation and Error Analysis.* Dordrecht, The Netherlands: Kluwer Academic Publishers, 2001.

[12] T. O. Sæbø, "Seafloor depth estimation by means of interferometric synthetic aperture sonar," Ph.D. dissertation, University of Tromsø, 2010.

[13] J. A. Ogilvy, *Theory of Wave Scattering from Random Rough Surfaces.* A. Hilger, 1991.

[14] C. S. Clay and H. Medwin, *Acoustical Oceanography: Principles and Applications.* John Wiley & Sons, 1977.

[15] L. Brekhovskikh and Y. Lysanov, *Fundamentals of Ocean Acoustics*, ser. Springer Series in Electrophysics. Springer-Verlag, 1982, vol. 8.

[16] R. J. Urick, *Principles of Underwater Sound.* Mcgraw-Hill Book Company, 1983.

[17] H. L. Van Trees, *Detection, estimation and modulation theory IV: Otpimum Array Processing.* John Wiley and Sons, Inc., 2003.

[18] K. W. Lo, "Adaptive array processing for wide-band active sonars," *IEEE J. Oceanic Eng.*, vol. 29, no. 3, pp. 837 – 846, Jul. 2004.

[19] C.-I. C. Nilsen, "Beamformers with applications in medical ultrasound imaging," Ph.D. dissertation, University of Oslo, 2010.

[20] J. Capon, "High-resolution frequency-wavenumber spectrum analysis," *Proc. IEEE*, vol. 57, no. 8, pp. 1408–1418, Aug. 1969.

[21] B. Widrow, K. Duvall, R. Gooch, and W. Newman, "Signal cancellation phenomena in adaptive antennas: Causes and cures," *IEEE Trans. on Antennas and Propagation*, vol. 33, no. 3, pp. 469 – 478, May 1982.

[22] J. F. Synnevåg, "Adaptive beamforming for medical ultrasound imaging," Ph.D. dissertation, University of Oslo, 2009.

[23] H. Cox, R. Zeskind, and M. Owen, "Robust adaptive beamforming," *IEEE Trans. Acoust., Speech, Signal Process.*, vol. 35, no. 10, pp. 1365 – 1376, Oct. 1987.

[24] B. D. Carlson, "Covariance matrix estimation errors and diagonal loading in adaptive arrays," *IEEE Trans. Aerosp. Electron. Syst.*, vol. 24, pp. 397–401, Jul. 1988.

[25] P. Stoica, H. Li, and J. Li, "A new derivation of the APES filter," *IEEE Signal Process. Lett.*, vol. 6, no. 8, pp. 205 –206, Aug. 1999.

[26] J.-F. Synnevåg, S. Holm, and A. Austeng, "A low complexity data-dependent beamformer," in *Ultrasonics Symposium, 2008. IUS 2008. IEEE*, Nov. 2008, pp. 1084 –1087.

[27] S. McDaniel, "Spatial covariance and adaptive beam forming of high-frequency acoustic signals forward scattered from the sea surface," *IEEE J. Oceanic Eng.*, vol. 16, no. 4, pp. 415–419, Oct. 1991.

[28] A. M. Rao and D. L. Jones, "Efficient detection with arrays in the presence of angular spreading," *IEEE Trans. Signal Processing*, vol. 51, no. 2, pp. 301 – 312, Feb. 2003.

[29] G. Montalbano and G. V. Serebryakov, "Optimum array signal processing in the presence of imperfect spatial coherence of wavefronts," in *OCEANS '98 Conference Proceedings*, vol. 3, Jun. 1998, pp. 1704 –1708.

[30] K. W. Hollman, K. W. Rigby, and M. O'Donnell, "Coherence factor of speckle from a multi-row probe," in *Proc. IEEE Ultrason. Symp*, vol. 2, Oct. 1999, pp. 1257 –1260.

[31] P. C. Li and M. L. Li, "Adaptive imaging using the generalized coherence factor," *IEEE Trans. Ultrason. Ferroelect. Freq. Contr.*, vol. 50, no. 2, pp. 128 –141, Feb. 2003.

[32] R. Mallart and M. Fink, "Adaptive focusing in scattering media through sound-speed inhomogeneities: The van Cittert Zernike approach and focusing criterion," *J. of the Acoustical Society of America*, vol. 96, no. 6, pp. 3721–3732, Jul. 1994.

[33] N. S. Neidell and M. T. Taner, "Semblance and other coherency measures for multichannel data," *Geophysics*, vol. 36, no. 3, pp. 482–497, Jun. 1971.

[34] K. Lau and Y. H. Leun, "Optimum beamformers for uniform circular arrays in a correlated signal environment," *Proc. IEEE Int. Conf. Acoust., Speech and Signal Proc.*, pp. 3093–3096, 2000.

[35] B. K. Lau, "Applications of adaptive antennas in third-generation mobile communications systems," Ph.D. dissertation, Curtin University of Technology, 2002.

[36] B. Friedlander, "Direction finding using an interpolated array," in *Proc. IEEE Int. Conf. Acoust., Speech and Signal Proc.*, vol. 5, apr 1990, pp. 2951 –2954.

[37] M. Born and E. Wolf, *Principles of Optics*, 7th ed. Cambridge, UK: Pergamon press, 1999.

[38] S. L. Wang and P. C. Li, "MVDR-based coherence weighting for high-frame-rate adaptive imaging," *IEEE Trans. Ultrason., Ferroelectr., Freq. Control*, vol. 56, no. 10, pp. 2097 – 2110, Oct. 2009.

[39] A. Jakobsson and P. Stoica, "Combining Capon and APES for estimation of spectral lines," in *Circuits, Systems, and Signal Processing*, vol. 19, no. 2, 1999.

Paper I

APES Beamforming Applied to Medical Ultrasound Imaging

A. E. A. Blomberg, I. K. Holfort, A. Austeng, J.-F. Synnevåg,
S. Holm and J. A. Jensen

Proc. IEEE Ultrasonics symposium, Rome, 2009.

APES Beamforming Applied to Medical Ultrasound Imaging

A. E. A. Blomberg, I. K. Holfort, A. Austeng, J.-F. Synnevåg,
S. Holm and J. A. Jensen

Abstract– Recently, adaptive beamformers have been introduced to medical ultrasound imaging. The primary focus has been on the minimum variance (MV) (or Capon) beamformer. This work investigates an alternative but closely related beamformer, the Amplitude and Phase Estimation (APES) beamformer. APES offers added robustness at the expense of a slightly lower resolution. The purpose of this study was to evaluate the performance of the APES beamformer on medical imaging data, since correct amplitude estimation often is just as important as spatial resolution. In our simulations we have used a 3.5 MHz, 96 element linear transducer array. When imaging two closely spaced point targets, APES displays nearly the same resolution as the MV, and at the same time improved amplitude control. When imaging cysts in speckle, APES offers speckle statistics similar to that of the DAS, without the need for temporal averaging.

I. INTRODUCTION

The minimum variance (MV) beamformer was originally used in passive systems for e.g. direction finding [1], and later extended to active systems such as medical ultrasound imaging [2], [3], [4]. It has been shown that the MV beamformer, when used with the right parameters, significantly improves the image resolution compared to the conventional delay-and-sum (DAS) beamformer. However, the MV is sensitive to errors in the steering vector and also suffers from signal cancellation in the case of coherent sources. Diagonal loading [5] and sub-array averaging [6] are necessary in order to address these issues. Still, the MV tends to under-estimate the amplitude of scatterers in some cases.

The closely related Amplitude and Phase Estimation (APES) beamformer was developed for improved amplitude control at the expense of slightly lower resolution. In [7], it is shown that APES is more robust against sound speed errors than MV when imaging single point targets. In this work, we have investigated the performance of the APES beamformer when imaging single and double point targets, as well as a cyst phantom. We have compared the APES beamformer to the MV and the DAS beamformers, with respect to resolvability, beamwidth, amplitude control and speckle appearance and statistics. In this context, resolvability is defined as the relative difference between the peak amplitude of the two laterally spaced point targets and the saddle point between them.

II. METHODS

A. The DAS beamformer

In the conventional DAS beamformer, a time delay is applied to the received signal from each of the sensors to steer and focus the beam in a given direction, before coherently combining the signals. Given an array of M sensors, the output of a general beamformer may be written as

$$z\left[n\right] = \sum_{m=0}^{M-1} w_m^* y_m \left[n - \Delta_m\right], \tag{1}$$

where n denotes the time sample index and Δ_m is the time delay applied to sensor m. $y_m[n - \Delta_m]$ is the received and delayed signal at element m. The signal received at each sensor is multiplied by a weight, w_m. In conventional, non-adaptive beamformers such as DAS, these weights are pre-defined and thus data-independent. Often, the sensor weights are defined by a window function such as a Hanning or a Kaiser window.

B. The MV beamformer

The MV beamformer differs from the DAS beamformer in the way in which the weights, w_m in (1), are calculated. Instead of using a set of pre-defined weights, the MV beamformer uses the recorded data field in order to compute the weights which minimize the variance of the output from the beamformer, while maintaining unit gain in the direction of interest. The MV beamformer computes the aperture weights by solving the following minimization problem [1]

$$\min_{\mathbf{w}} \mathbf{w}[n]^H \hat{\mathbf{R}}[n]\mathbf{w}[n] \text{ subject to } \mathbf{w}[n]^H \ \mathbf{a} = 1, \tag{2}$$

where $\mathbf{w}$ is an Mx1 vector containing the complex sensor weights, $\hat{\mathbf{R}}$ is the estimated spatial covariance matrix, and $\mathbf{a}$ is the *steering vector*. Eq. (2) has an analytical solution given by

$$\mathbf{w}_{MV}[n] = \frac{\hat{\mathbf{R}}[n]^{-1}\mathbf{a}}{\mathbf{a}^H \hat{\mathbf{R}}[n]^{-1}\mathbf{a}}. \tag{3}$$

In active imaging systems, sub-array averaging is used to address the problem of signal cancellation caused by coherent sources. This involves dividing the transducer array into sub-arrays of length L, computing the spatial covariance matrix of each of the sub-arrays and using the averaged covariance matrix in (3). The parameter L should be chosen with care, as discussed in [3] and [4]. While long sub-arrays result in improved resolution, shorter sub-arrays tend to give more robust amplitude estimates. Diagonal loading, i.e. adding a small amount of energy to the diagonal of the covariance matrix, is often necessary to ensure an invertible and robust estimate of the covariance matrix.

C. The APES beamformer

The APES beamformer is designed such that the output is as close as possible to a plane wave with wavenumber k_x, where k_x represents the direction in which the beam is steered. The APES beamformer computes the weights which solve the following minimization problem

$$\begin{aligned} \min_{\mathbf{w},\alpha} \frac{1}{M-L+1} \sum_{m=0}^{M-L+1} |w^H y_m\left[n-\Delta_m\right] - \alpha e^{jk_x x_m}|^2 \\ \text{subject to } \mathbf{w}[n]^H \mathbf{a} = 1, \end{aligned} \tag{4}$$

where $y_m\left[n-\Delta_m\right]$ is the received and delayed signal, n denotes the time sample index, $\mathbf{w}$ is a vector of apodization weights, m denotes the element number, x_m is the x-coordinate of element m and α is the complex amplitude of the desired plane wave. Let $G(k_x) = \frac{1}{M}\sum_{m=0}^{M-1} y_m\left[n-\Delta_m\right] e^{-jk_x x_m}$. The expression to be minimized in (4) can be re-written as [8]

$$\begin{aligned} &\frac{1}{M-L+1} \sum_{m=0}^{M-L} |w^H y_m\left[n-\Delta_m\right] - \alpha e^{jk_x x_m}|^2 \\ &= \mathbf{w}^H \hat{\mathbf{R}}\mathbf{w} - \alpha^* \mathbf{w}^H \mathbf{G}(k_x) - \alpha \mathbf{G}^H(k_x)\mathbf{w} + |\alpha|^2 \\ &= |\alpha - \mathbf{w}^H \mathbf{G}(k_x)|^2 + \mathbf{w}^H \hat{\mathbf{R}}\mathbf{w} - |\mathbf{w}^H \mathbf{G}(k_x)|^2. \end{aligned} \tag{5}$$

Minimizing (5) with respect to α, gives $\hat{\alpha} = \mathbf{w}^H G(k_x)$. Inserting this in (5) results in the following minimization problem

$$\min_{\mathbf{w}} \mathbf{w}^H \hat{\mathbf{Q}} \mathbf{w} \text{ subject to } \mathbf{w}[n]^H \mathbf{a} = 1, \tag{6}$$

where $\hat{\mathbf{Q}} = \hat{\mathbf{R}} - \mathbf{G}(k_x)\mathbf{G}^H(k_x)$. Eq. (6) has a solution given by [8]

$$\mathbf{w}_{APES} = \frac{\hat{\mathbf{Q}}^{-1}\mathbf{a}(k_x)}{\mathbf{a}^H(k_x)\hat{\mathbf{Q}}^{-1}\mathbf{a}(k_x)}. \tag{7}$$

The APES solution is equivalent in form to the MV solution, with the exception that the spatial covariance matrix, $\hat{\mathbf{R}}$, is replaced by $\hat{\mathbf{Q}}$, which may be interpreted as the noise covariance matrix.

III. Results and Discussion

We have used Field II [9], [10] for the simulations. Data was obtained for point targets and for a cyst phantom in speckle, using a 96-element, 3.5 MHz, 18.5 mm transducer. Dynamic focusing was used both on transmission and on reception. The cyst was modelled as a cylindrical area with a radius of 3 mm, within which the reflection coefficient of the scatterers is zero. Homogeneous tissue surrounding the cyst region was modelled by placing 350 000 randomly distributed point scatterers within a volume defined by a radial distance of 3 to 5 cm, a lateral angle of -90 ° to 90 ° and an elevation angle of -3.9 ° to 3.9 °, corresponding to the sezond zero point of the array beampattern. Two strong point reflectors were also placed inside the tissue region. Diagonal loading corresponding to $\frac{5\%}{L}$ of the received power was used, in accordance with previously recommended parameter sets [4].

Fig. 1 shows the steered response from two closely spaced point reflectors imaged using the DAS with uniform weighting (dashed line), the MV (solid line) and the APES (solid line with crosses) beamformer. The point reflectors are placed 3 mm apart, at a depth of 5 cm. In the leftmost plot, a sub-array length of L=24 is used, in the middle L=36 and on the right L = 48. For all choices of L, The MV and APES bamformers display significantly narrower mainlobes than the DAS, as well as better resolvability. Between the MV and the APES beamformers, the MV displays the narrowest mainlobe and the highest resolvability. The performance of the MV and the APES beamformers are similar for short sub-arrays (L=24). As the sub-array length increases, the performance of the APES beamformer stays relatively constant while the MV displays increasing resolvability and a narrower mainlobe, at the expense of less robust amplitude estimates (under-estimated by up to 5 dB). In Fig. 2, the resolvability (left), full width at half maximum (FWHM) (middle), and normalized peak amplitude (right) for each of the beamformers are plotted for sub-array lengths ranging from 24 to 48 in steps of 4. The DAS beamformer is able to resolve the two points by 17 dB, while the APES beamformer resolves them by about 19 B. For the MV, the resolvability improves significantly with the sub-array length, resolving the points by about 20 dB (L=24) to 25 dB (L=48). The FWHM values for the APES and MV beamformers are both much smaller than for the DAS beamformer, but again the MV beamformer shows a slightly narrower mainlobe than the APES beamformer. The peak amplitude of the APES beamformer stays nearly constant and very close to that of DAS, while it drops down to 5 dB (L=48) below that of the DAS, for the MV.

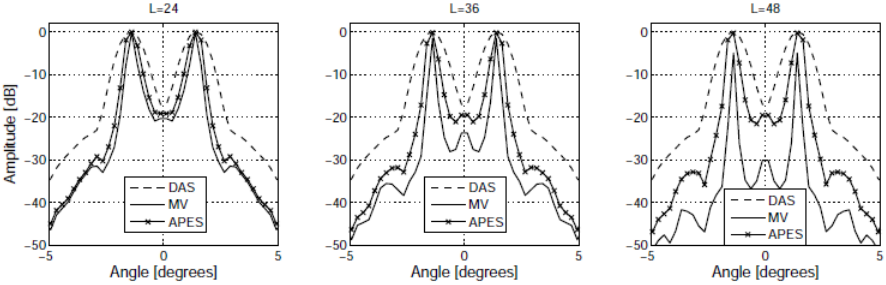

Fig. 1: *Steered response for the DAS (dashed), the MV (solid) and the APES (solid with crosses) beamformers, with L=24 (left), L=36 (middle) andL=48 (right).A 3.5 MHz 96 element array was used. The point targets are placed at a depth of 5 cm.*

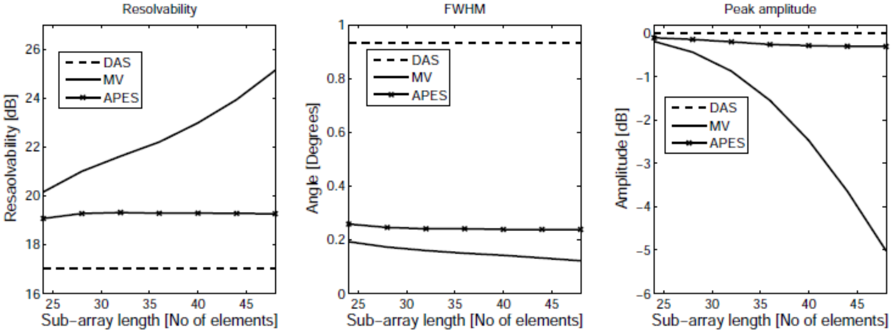

Fig. 2: *Resolvability (left), FWHM (middle) and normalized peak amplitude (right) for sub-array lengths from 24 to 48 in steps of four. The resolvability is measured as the relative distance between the peaks of two scatterers and the saddle point between them. FWHM is measured from the response of a single point scatterer. The peak amplitude is computed for double point reflectors ans is normalized by the peak amplitude of the DAS beamformer.*

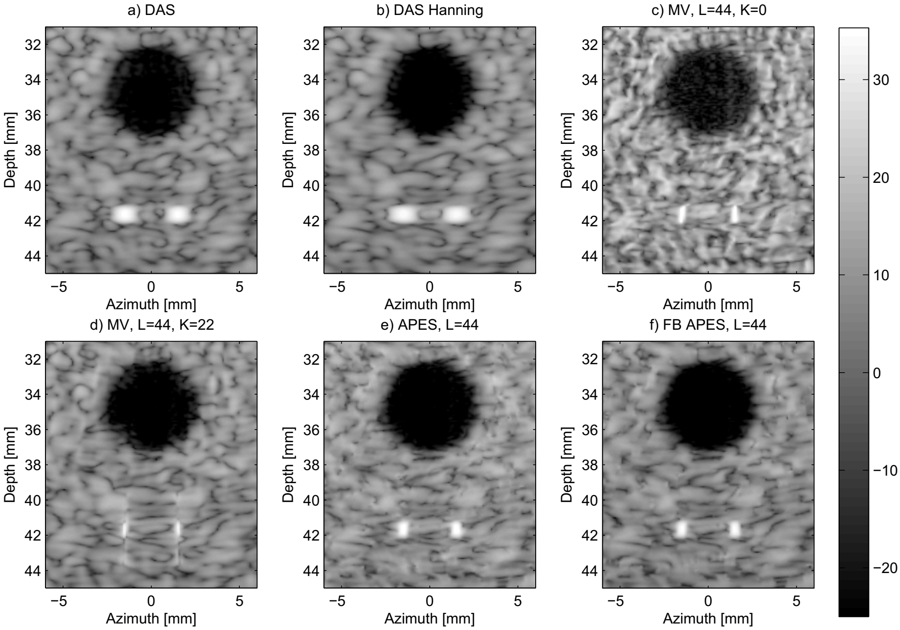

Fig. 3: *A simulated cyst phantom in speckle together with two strong reflectors, imaged using a 96 element, 18.5 mm, 3.5 MHz transducer. Each image is normalized by its mean speckle value. (a): DAS with a rectangular window, (b): MV with temporal averaging over one pulse length, (c): MV with temporal averaging over one pulse-length, (d): APES, (e): Forward-backward APES.*

In medical ultrasound imaging, resolution and contrast as well as reliable amplitude estimates are of importance. Also, the speckle pattern caused by scattering from micro-structures within the tissue may be of clinical interest. Fig. 3 shows a cyst phantom in speckle together with two strong point reflectors. The DAS beamformer with a rectangular window (a), and with a Hanning window (b) result in some smearing of the point reflectors, as expected due to the wide mainlobe of the conventional beamformer. The Hanning window in (b) reduces the sidelobes, resulting in less energy leakage into the cyst region, but the resolution is decreased as can be seen from the point reflectors. The MV beamformer (c) gives well-defined point targets, but there is considerable leakage into the cyst region, and the speckle pattern looks quite different from what could be expected.

Temporal averaging (as in (d) where averaging over one pulse length is used) has been suggested as a way to improve the speckle statistics when using the MV [11]. The APES beamformer (e) results in a clear definition of the edges of the cyst as well as the point reflectors. Also, there is less energy leakage from sidelobes. The increased amplitude control of the APES beamformer results in a speckle pattern similar to that of the DAS beamformer, without the need for temporal averaging. Forward-backward averaging has been proposed by several authors, see e.g. [12], in order to further improve the APES estimate. APES with forward-backward averaging is shown in e).

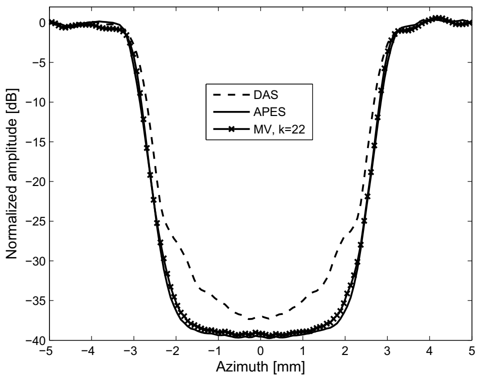

Fig. 4: *Horizontal slice through the center of the cyst, imaged using DAS rectangular window (dashed), APES (solid) and MV with temporal averaging (solid with crosses). Images from 100 simulations were averaged.*

To ensure stable results, we have run 100 simulations on a cluster of Linux workstations, randomly distributing the point scatterers each time. Fig. 4 shows a horizontal slice through the center of the cyst, created by averaging the images from the 100 simulations. 15 depth samples were averaged for each of the beamformers ((a), (d), and (e) from Fig. 3). Among these beamformers, APES provided the lowest value inside the cyst region together with the MV with temporal averaging, indicating a low amount of energy leakage into this area.

Speckle statistics are quantified using the pixel signal-to-noise ratio (SNR_p) (1.91 for fully developed speckle), defined as the mean value divided by the standard deviation within a speckle region [13]. Table I summarizes these values for each of the beamformers. The statistics in Table I are average values from the 100 simulations. These measurements show that the APES beamformer offers speckle statistics close to the theoretical value for fully developed speckle, without the need for temporal averaging. For the MV beamformer, temporal averaging over one pulse length is necessary in order to achieve speckle statistics comparable to that of the DAS.

Beamformer	mean	std	SNR_p
DAS	0.31	0.16	1.91
DAS Hanning	0.31	0.12	1.91
MV, K=0	0.16	0.13	1.21
MV, K=22	0.30	0.16	1.90
APES	0.28	0.14	1.91
FB APES	0.29	0.15	1.91

Table I: *Speckle statistics (mean, standard deviation and SNR_p) computed from a speckle region for each of the beamformers. The values are averaged over 100 realizations of speckle.*

IV. Conclusion

The APES beamformer may be preferable to the MV beamformer in applications where robustness and reliable amplitude estimates are of importance. The MV beamformer can achieve higher resolution than the APES beamformer, but it suffers from sensitivity to assumed parameters such as the propagation velocity, the choice of sub-array length and the amount of diagonal loading applied. The MV beamformer also suffers from signal cancellation in the presense of coherent sources, which is the case in an active system such as medical ultrasound imaging. Because of the way the minimization criterion is formulated in the APES beamformer, it does not suffer from signal cancellation to the same extent [12]. Also, the APES beamformer is less dependent on the choice of model parameters, and the improved amplitude control results in speckle patterns similar to that of the DAS beamformer. The computational burden of the APES beamformer is only marginally larger than that of the MV beamformer. The most demanding computational step of the MV and APES beamformers, is the matrix inversion in (3) and (7). Since the dimensions of the matrices $\hat{\mathbf{R}}$ and $\hat{\mathbf{Q}}$ are directly proportional to the sub-array lengths, L, using a shorter sub-array length will reduce the computational burden. As illustrated by Fig. 2, the performance of the APES beamformer is less dependent on L, so the sub-array length may be reduced without sacrificing performance. The fact that temporal averaging is unnecessary further reduces the number of computations. The APES beamformer is therefore a strong candidate for applications in medical ultrasound, offering high image resolution and contrast as well as robustness and speckle patterns similar to that of the DAS beamformer.

Bibliography

[1] J. Capon, "High-resolution frequency-wavenumber spectrum analysis," *Proc. IEEE*, pp. 1408–1418, August 1969.

[2] I. K. Holfort, F. G., and J. A. Jensen, "Broadband minimum variance beamforming for ultrasound imaging," *IEEE Trans. on Ultrason., Ferroelec., and Freq. Contr.*, February 2009.

[3] J.-F. Synnevåg, A. Austeng, and S. Holm, "Adaptive beamforming applied to medical ultrasound imaging," *IEEE Trans. Ultrason., Ferroelec., Freq. Contr.*, pp. 1606–1613, August 2007.

[4] ——, "Benefits of minimum variance beamformning in medical ultrasound imaging," *IEEE Trans. Ultrason., Ferroelec., Freq. Contr.*, September 2009.

[5] T.-J. Shan, M. Wax, and T. Kailath, "On spatial smoothing for direction-of-arrival estimation of coherent signals," *IEEE Trans. Acoust., Speech, Signal Process.*, pp. 806–811, August 1985.

[6] T.-J. Shan and T. Kailah, "Adaptive beamforming for coherent signals and interference," *IEEE Trans. Acoust., Speech, Signal Process.*, pp. 527–536, June 1985.

[7] I. K. Holfort, F. Gran, and J. A. Jensen, "Investigation of sound speed errors in adaptive beamforming," in *Proc. IEEE Ultrason. Symp.*, 2008.

[8] P. Stoica, H. Li, and J. Li, "A new derivation of the apes filter," *IEEE Signal Processing Letters*, August 1999.

[9] J. A. Jensen and N. B. Svendsen, "Calculation of pressure fields from arbitrarily shaped, apodized, and excited ultrasound transducers," *IEEE Trans. Ultrason., Ferroelec., Freq. Contr.*, pp. 262–267, 1992.

[10] J. A. Jensen, "A program for simulating ultrasound systems," *Med. Biol. Eng. Comp., vol. 10th Nordic-Baltic Conference on Biomedical Imaging*, pp. 351–353, 1996.

[11] J.-F. Synnevåg, C. I. C. Nilsen, and S. Holm, "Speckle statistics in adaptive beamforming," *Proc. IEEE Ultrason. Symp.*, pp. 1545–1548, October 2007.

[12] A. Jakobsson and P. Stoica, "On the forward-backward spatial APES," *Signal Process.*, vol. 86, no. 4, pp. 710–715, 2006.

[13] J. M. Thijssen, G. Weijers, and C. L. de Korte, “Objective performance testing and quality assurance of medical ultrasound equipment,” *Ultrasound in Med. & Biol.*, pp. 460–471, March 2007.

Paper II

Adaptive Beamforming Applied to a Cylindrical Sonar Array using an Interpolated Array Transformation

A. E. A. Blomberg, A. Austeng and R. E. Hansen

IEEE Journal of Oceanic Engineering
Accepted for publication Sep. 14, 2011.

Adaptive Beamforming Applied to a Cylindrical Sonar Array using an Interpolated Array Transformation

A. E. A. Blomberg, A. Austeng and R. E. Hansen

Abstract– In applications such as fishery sonar and navigation, cylindrical or spherical arrays are often used because of the need for a 360 degree field of view. However, adaptive beamforming methods, known for their high angular resolution and interference rejection capabilities, often rely on a Vandermonde structure of the steering vectors. This is generally not the case for non-linear arrays. In this work we use an interpolated array tranformation to map the data to a virtual linear array prior to adaptive beamforming. We evaluate the performance of two different adaptive beamformers using simulations as well as experimental data from the SX90 fish finding sonar. We show that the adaptive Minimum Variance (MV) and Amplitude and Phase Estimation of a Sinusoid (APES) beamformers offer a significant improvement in azimuth resolution compared to the conventional delay-and-sum (DAS) beamformer. The APES beamformer offers slightly more reliable amplitude estimates in the direction of interest compared to the MV beamformer, at the cost of a somewhat lower azimuth resolution. When applied to data from the SX90 fish finding sonar, the MV beamformer offers a 40-50% improvement in resolution, while the APES beamformer offers an improvement of 20-30%.

I. INTRODUCTION

The standard beamforming method in sonar imaging today is delay-and-sum (DAS). The DAS beamforming method is non-adaptive in the sense that the sensor weights are pre-defined [1]. In recent decades, adaptive beamforming methods have been introduced. Instead of using pre-defined weights, these methods use the recorded wavefield to compute a set of sensor weights which are optimal in some sense. Under the right conditions, adaptive beamforming methods are known to offer a significant improvement in angular resolution as well as the ability to suppress interfering signals, compared to their non-adaptive counterpart. One of the first publications on adaptive beamforming was by Bryn [2] in 1962, who used adaptive beamforming for optimal signal detection using three-dimensional arrays. In 1969, Capon used adaptive beamforming for improved localization of earthquakes [3]. These works showed how adaptive beamforming could be used for improved performance in *passive* systems. In *active* systems, adaptive methods such as the standard Minimum Variance (MV) beamformer fail because they lack the ability to handle coherent signals [4]. If not properly addressed, signal cancellation may cause severe underestimation of the signal amplitudes. Correct amplitude estimates are of importance particularly in imaging applications such as fishery sonar, where the target strength contains information about the type and quantity of fish.

Subaperture pre-beamforming, i. e., dividing the physical array into subapertures which are pre-beamformed using a conventional beamformer prior to adaptive beamforming, has been proposed as a means of reducing the complexity of adaptive beamformers [5, 6]. This is sometimes referred to as partially adaptive beamforming. The pre-beamforming step implicitly suppresses interfering signals and noise, and was successfully used in [7, 8] in conjunction with adaptive beamforming in an active environment.

In 1985, Shan and Kailath proposed a spatial averaging, or subarray averaging technique, which explicitly addresses the signal cancellation problem by decorrelating coherent sources [9]. Today, subarray averaging is widely used to make adaptive methods robust in an active environment with coherent echoes. It is used for instance by Lo in [10], where the author illustrates improved performance of several adaptive beamformers when applied to an active sonar system.

The subarray averaging technique was developed for uniformly sampled linear arrays (ULAs) with steering vectors displaying a so-called Vandermonde structure. In many sonar applications such as surveillance and fishery sonar, the need for a 360 degree field of view implies that spherical or cylindrical arrays are more suitable than linear ones. When the array is curved, the impinging wavefield will appear different from subarray to subarray, and the subarray averaging technique will not work properly. *Interpolated array transformations*, such as the ones proposed by Cook et. al. [11], Bronez [12] and Friedlander [13] have been developed to transform the steering vector of an arbitrary planar array into a Vandermonde structure amenable to subarray averaging. In [14], [15], and recently in [16, 17], interpolated array transformations are used in the context of direction of arrival (DOA) estimation, while in [18] the authors apply an interpolated array transformation to measured seismic data for source localization. In [19], the authors use an interpolated array transformation to account for mutual coupling and other system errors prior to adaptive beamforming using a conformal array.

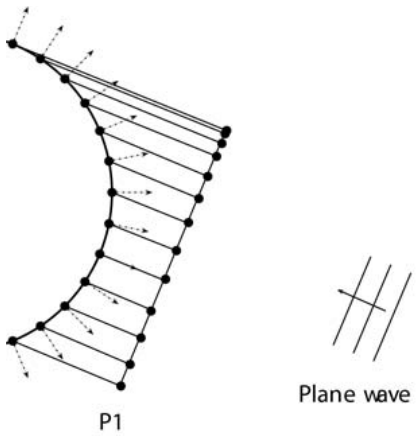

Fig. 1: *After delaying the signal at each receiver to steer the beam in the desired direction, subarray averaging can be applied to the data at plane P1. However, at this stage the data is non-uniformly sampled, and each subarray consists of elements with different directivity, as indicated by the arrows.*

In this paper the focus is on active sonar imaging. Although the theoretical framework for applying adaptive beamformers to arbitrarily shaped sonar arrays is in place, there are, to the authors' knowledge, no published works evaluating the performance of these methods in practice. In this work we use simulated as well as experimental data to evaluate the performance of two different adaptive beamfomers applied to a cylindrical sonar array. We show that when applying an interpolated array transformation prior to beamforming, adaptive beamforming methods offer improved resolution and lower or comparable sidelobe levels compared to conventional beamforming methods. The APES beamformer offers more correct amplitude estimates in the direction of interest compared to the MV beamformer, at the cost of a somewhat lower azimuth resolution.

In Section II. A we describe the transformation proposed by Friedlander (from now on referred to as the Friedlander transformation) to map the data from a curved array to a virtual ULA, and explain how it is applied prior to beamforming. The conventional DAS beamformer as well as the adaptive Minimum Variance (MV) and the Amplitude and Phase Estimation of a Sinusoid (APES) beamformers are outlined in Section II. B. In Section III. A we present results from simulations and verify them using experimental data from the Simrad SX90 sonar in Section III. B. When applied to an experimental setting, the MV beamfomer offers an increase in azimuth resolution of 40 to 50%, while the APES beamformer offers an improvement of about 20 to 30%, when compared to the conventional method. Finally, we offer a brief summary in Section IV.

II. METHODS

We start by explaining the concept of interpolated array transformations in Section II. A and outline how the Friedlander transformation can be applied to a circular or cylindrical array to map the data to a virtual ULA prior to beamforming. In Section II. B, we describe the

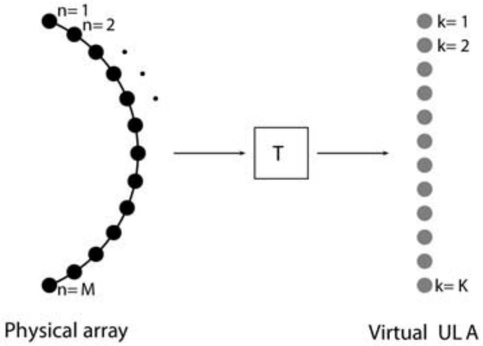

Fig. 2: *An interpolated array transformation maps the data from a physical curved array to a virtual ULA.*

conventional DAS and the adaptive MV and APES beamformers.

A. Interpolated array transformation

ULAs have received by far the most attention in research concerning conventional and adaptive beamforming. Many array processing techniques, including subarray averaging, rely on the Vandermonde structure of the steering vector of the ULA. Figure 1 illustrates why the subarray averaging technique, where the physical array is divided into several overlapping segments and the covariance matrix from each subarray is averaged, cannot be applied directly to a curved array. After delaying the signals from each receiver to steer in the direction of the impinging plane wave, the data along the plane P1 is non-uniformly sampled in space and consists of data from sensors with different directivity.

Interpolated array transformations have been proposed to transform the output of a non-ULA type array into a form to which subarray averaging and other processing techniques developed for ULAs can be applied. An overview and comprehensive description of these is given in [20]. The most widely used method is the one proposed by Friedlander [13], or a variety of this.

Fig. 2 illustrates the concept of an interpolated array transformation. The output from a physical array is transformed by a transformation **T**, onto a virtual array. We will denote the steering vector of the physical array **a** and the target steering vector of the virtual ULA **b**. The steering vector of an M-element array is defined as $\mathbf{a}(\mathbf{k}) = [e^{-j\mathbf{k}^T\mathbf{p}_1}...e^{-j\mathbf{k}^T\mathbf{p}_M}]^T$, where **k** is the wavenumber vector and **p** is a vector of element locations. Often the virtual array is chosen to be a ULA with a steering vector displaying the desired Vandermonde structure, i.e., it is linear in $\sin\theta$ (θ being the steering direction of the beamformer). Since the difference in the steering vectors of the physical and interpolated array may be large, the transformation is only applied to a sector of angles (the in-sector). The process thus needs to be repeated several times to get full azimuth coverage. Generally, the transformation error increases with the size of the in-sector since the virtual array is a compromise over the whole sector. At the same time, a small in-sector can result in incorrect DOA estimates if there are coherent signals impinging on the array from outside the in-sector. The size of the transmit beam and the element directivity are factors to be taken into account when determining the size of the in-sector, since they determine the region from which to expect significant energy. With an array consisting of omni-directional elements the out-of-sector response can degrade the system performance if it is not taken into account [11,16,20]. When using directive elements, energy arriving from directions outside the imaging sector are implicitly suppressed because of the directivity of the receiver, and the need for controlling the out-of-sector response is reduced.

Let $\mathbf{B} = [\mathbf{b}(\mathbf{k}_1) \cdots \mathbf{b}(\mathbf{k}_S)]$ be the $K \times S$ matrix of target steering vectors of the virtual ULA and $\mathbf{A} = [\mathbf{a}(\mathbf{k}_1) \cdots \mathbf{a}(\mathbf{k}_S)]$ the $M \times S$ matrix of steering vectors of the physical array, where S is the number of discrete angles within the in-sector, and M and K are the number of elements in the physical and virtual arrays, respectively. Further, let $\mathbf{G}$ be an $M \times S$ matrix containing the directional response of each element in the physical array, and $\bar{\mathbf{A}} = \mathbf{G} \cdot \mathbf{A}$ contain the steering vectors of the physical array with element directivity taken into account, where $(\cdot)$ denotes element by element multiplication. The Friedlander transformation matches the steering vectors of the physical array to those of the virtual ULA in a least squares sense, for each steering angle within the in-sector.

$$\mathbf{T} = \arg\min_{\mathbf{T}} \parallel \mathbf{T}\bar{\mathbf{A}} - \mathbf{B} \parallel_F^2, \tag{1}$$

where F denotes the Frobenius norm. The solution to Eq. (1) is

$$\mathbf{T} = \mathbf{B}\bar{\mathbf{A}}^{\dagger}, \tag{2}$$

where † denotes the Moore-Penrose pseudo-inverse operation [21],

$$\bar{\mathbf{A}}^{\dagger} = \bar{\mathbf{A}}^{H}(\bar{\mathbf{A}}\bar{\mathbf{A}}^{H})^{-1} \tag{3}$$

It is common to choose $K < M$ to ensure that Eq. (2) is well conditioned [20]. To transform the complex samples received by the physical array into a form to which subarray averaging can be applied, the output from the physical array, $\mathbf{x}$, is transformed using $\mathbf{T}$.

$$\mathbf{y} = \mathbf{T}\,\mathbf{x}. \tag{4}$$

Beamforming can then be applied to the transformed data, $\mathbf{y}$. The transformation matrix, $\mathbf{T}$, can be computed offline. Thus the increase in computational burden is small.

B. Beamforming

Consider a uniformly sampled circular array with $M = 32$ elements and radius r, as shown in Fig. 3. The elements are directive, and not all elements receive signals from all directions because of the circular geometry of the array. Consequently only a sector, or sub-aperture, is used at a time for beamforming. In subsequent examples, we use sub-apertures of $M = 13$ physical elements. Numbering the elements from 1 to 32, elements 3 to 15 are active when steering toward $\theta = 0$ and elements 7 to 19 when steering toward $\theta = \pi/4$, etc. The virtual ULA is placed perpendicular to the steering direction as illustrated by Fig. 3.

We are operating in the far field such that the impinging waves are assumed plane. Assuming q narrowband sources arriving from q distinct directions, the $M \times 1$ vector received by the

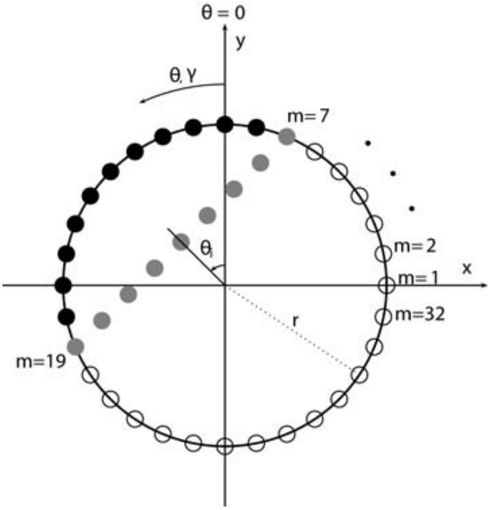

Fig. 3: *The angular position of each element, γ, and the steering angle, θ are defined counter-clockwise from the positive y-axis. When steering toward $\theta_i = \pi/4$, elements 7 to 19 are active. The corresponding virtual ULA is shown in gray.*

physical array at time sample n may be expressed as

$$\mathbf{x}[n] = \sum_{k=1}^{q} \bar{\mathbf{a}}[\theta_k] s_k[n] + \mathbf{n}[n] = \sum_{k=1}^{q} (\mathbf{g}[\theta_k] \cdot \mathbf{a}[\theta_k]) s_k[n] + \mathbf{n}[n], \tag{5}$$

where $\mathbf{g}[\theta_k]$ is an M-dimensional vector containing the directional response to a signal impinging from direction θ, s_k is the signal from source k and $\mathbf{n}$ denotes noise. For a plane wave with wavelength λ arriving from azimuth angle θ and elevation angle ϕ, the M-dimensional steering vector is given by

$$\mathbf{a} = [e^{-jkr\sin(\phi)\cos(\theta-\gamma_1)}, ..., e^{-jkr\sin(\phi)\cos(\theta-\gamma_M)}]^T, \tag{6}$$

where the steering direction, θ, and the angular position of element m, given by $\gamma_m = 2\pi(m - 1/M)$ for $m = 1, ..., M$, are defined anti-clockwise from the positive y-axis. The origin is defined as the center of the array and $\mathbf{k}$ is the wavenumber vector $[k_x, k_y, k_z]$, $k = |\mathbf{k}| = \frac{2\pi}{\lambda}$. From here on the elevation angle is assumed to be $\pi/2$, i.e., the signals impinging on the array are in the same plane as the array. For circular elements as the ones in Fig 3, the directional response for each element with radius r is given by

$$g_m(\theta) = \frac{2J_1(kr\sin(\theta-\gamma_m))}{kr\sin(\theta-\gamma_m))}, \tag{7}$$

where $J_1()$ denotes the first-order Bessel function of the first kind [22, chapter 4].

The steering vector of the virtual ULA in Fig. 3 is given by

$$\mathbf{b} = [e^{jk(\sin\theta p_{x1}+\cos\theta p_{y1})}, ..., e^{jk(\sin\theta p_{xK}+\cos\theta p_{yK})}]^T, \tag{8}$$

where p_{xi} and p_{yi} are the x- and y-positions of element i in the K-element virtual ULA. We have chosen to position the virtual ULA along the chord of the physical array, as illustrated by Fig. 3. The complex data samples received by the physical array are transformed using Eq. (4) prior to beamforming.

1) The DAS beamformer: The delay-and-sum (DAS) beamformer applies a time delay (or equivalently a phase delay the narrowband case) to the received signal from each of the sensors to steer and focus the beam. A set of sensor weights are applied before coherently combining the signals from each of the sensors. Given an array of K sensors, the output of a general beamformer may be written as

$$z\left[n\right] = \sum_{k=0}^{K-1} w_k^* y_k \left[n - \Delta_k\right], \tag{9}$$

where n denotes the time sample index, Δ_k is the time delay applied to sensor k, $y_k[n - \Delta_k]$ is the received and delayed signal at element k, and w_k^* denotes the weight for sensor k. In the conventional DAS beamformer, the weights are pre-defined, often by a window function such as a Hann or a Kaiser window [22, chapter 3]. Depending on the chosen window function, features of the beampattern such as the mainlobe width, sidelobe levels and positions of the nulls are defined once and for all. This is not the case for adaptive beamformers.

2) The MV beamformer: The key to the MV beamformer is that it adapts to the data; suppressing interfering signals from off-axis directions and allowing large sidelobes in areas where there is little energy. This results in potentially improved image quality, with improved resolution and less reverberations and cluttering effects. The MV weights are chosen such that the variance of the output from the beamformer is minimized while maintaining unity gain the direction of interest.

The MV beamformer computes the aperture weights by solving the following minimization problem [3]

$$\min_{\mathbf{w}} \mathbf{w}[n]^H \mathbf{R}[n] \mathbf{w}[n] \text{ subject to } \mathbf{w}[n]^H \mathbf{b} = 1, \tag{10}$$

where $\mathbf{w}[n]$ is an Kx1 vector containing the sensor weights for time sample n, $\mathbf{R}$ is the spatial covariance matrix, and $\mathbf{b}$ is the target steering vector of the interpolated array. Since the received signals have already been steered using a delay in Eq. (1), $\mathbf{b}$ is now a vector of ones. Note that the sensor weights, $\mathbf{w}$, may be complex valued. Eq. (2) can be solved using Lagrange multipliers [4], [22, chapter 6] and has an analytical solution given by

$$\mathbf{w}[n] = \frac{\mathbf{R}[n]^{-1}\mathbf{b}}{\mathbf{b}^H \mathbf{R}[n]^{-1}\mathbf{b}}. \tag{11}$$

Eq. (3) needs to be solved for each steering direction and time (or range) sample, since the optimal MV weights vary from pixel to pixel in the image. In practice the spatial covariance matrix, $\mathbf{R}$, in Eq. (3) must be replaced by its estimate, $\hat{\mathbf{R}}$.

In a coherent environment, the MV beamformer may suffer from *signal cancellation*, resulting in an underestimation of the amplitude of the desired signal [23]. In the worst possible case of two perfectly coherent sources, the amplitude of the desired signal is reduced to only 3 dB above the background level [1, chapter 7.3.4]. Subarray averaging has been proposed as a means of estimating the spatial covariance matrix by dividing the transducer array into subarrays of length L, computing the spatial covariance matrix of each of the subarrays and using the averaged covariance matrix in Eq. (3). Subarray averaging effectively decorrelates the coherent signals, reducing or completely mitigating the signal cancellation effect [1, chapter 7.3.4], [24]. As such it is an essential processing step when adapting the MV beamformer to an active signal environment. The estimated covariance matrix using subarray averaging can be expressed as

$$\hat{\mathbf{R}}[n] = \frac{1}{K-L+1} \sum_{l=0}^{K-L} \mathbf{y}_l[n]\mathbf{y}_l^H[n], \tag{12}$$

where $\mathbf{y}$ contains the delayed measurements from the sensors in subarray l.

The choice of the subarray length, L, implies a tradeoff between robustness and resolution. Since the number of degrees of freedom in the MV beamformer is equal to L, a longer subarray implies more degrees of freedom with which to suppress interfering signals and obtain the best possible resolution. Choosing a smaller L implies more spatial averaging and a solution which is more robust against signal cancellation, at the cost of a lower resolution [24–26].

Diagonal loading was originally developed to make adaptive beamforming methods more robust at the cost of a somewhat lower resolution [27, 28]. It involves adding a constant, ϵ, to the diagonal of the covariance matrix such that $\hat{\mathbf{R}}[n]$ is replaced by $\hat{\mathbf{R}}[n] + \epsilon\mathbf{I}$. We have chosen ϵ to be proportional to the power of the observations such that

$$\epsilon = \frac{\Delta tr\left\{\mathbf{R}[n]\right\}}{L}, \tag{13}$$

where $tr\left\{.\right\}$ is the trace operator. The MV amplitude estimate is then found by applying the optimal weights from Eq. (3) to the delayed data from each of the $K - L + 1$ subarrays and averaging over all subarrays

$$\mathbf{z}_{MV}[n] = \frac{1}{K-L+1} \sum_{l=0}^{K-L} \mathbf{w}[n]^H \mathbf{y}_l[n]. \tag{14}$$

3) The APES beamformer: The APES beamformer is closely related to the MV beamformer, but was developed for improved amplitude control and added robustness at the expense of a slightly lower resolution. Several derivations of the APES beamformer have been proposed, the one outlined in this section is derived in [29]. The APES beamformer computes the weights which solve the following minimization problem

$$\min_{\mathbf{w},\alpha} \frac{1}{K-L+1} \sum_{l=0}^{K-L} |\mathbf{w}^H \mathbf{y}_l - \alpha e^{jk_x \bar{x}_l}|^2 \quad \text{subject to } \mathbf{w}^H \mathbf{b} = 1, \tag{15}$$

where $\mathbf{y}_l$ is a vector containing the delayed measurements from subarray l, $\mathbf{w}$ is a vector of weights, $\bar{x}_l$ is the phase center of subarray l and α is the complex amplitude of the desired signal. $\mathbf{b}$ is a vector of ones because of the pre-steering in Eq. (1). Eq.(15) has a solution given by [29]

$$\mathbf{w}_{APES}[n] = \frac{\hat{\mathbf{Q}}[n]^{-1}\mathbf{b}}{\mathbf{b}^H\hat{\mathbf{Q}}[n]^{-1}\mathbf{b}}, \tag{16}$$

where $\hat{\mathbf{Q}} = \hat{\mathbf{R}} - \mathbf{g}(k_x)\mathbf{g}^H(k_x)$ and $\mathbf{g}$ is given by

$$\mathbf{g}(k_x) = \frac{1}{K-L+1}\sum_{l=0}^{K-L}\mathbf{y}_l e^{-jk_x\bar{x}_l}. \tag{17}$$

The APES solution is equivalent in form to the MV solution, with the exception that the spatial covariance matrix, $\hat{\mathbf{R}}$, is replaced by $\hat{\mathbf{Q}}$, which may be interpreted as the noise covariance matrix. Since the estimate of the desired signal is subtracted in Eq. (15), the APES beamformer is generally not affected by signal cancellation. Subarray averaging should still be applied to ensure a robust and invertible $\hat{\mathbf{Q}}$.

The improved resolution and interference rejection capabilities of the MV and APES adaptive beamformers comes at the cost of added computational complexity. While the complexity of the conventional DAS beamformer is in the order of O(K), K being the number of elements in the array, the complexity of the MV and APES beamformers is in the order of O(L^3).

III. Results and discussion

We have compared the performance of the DAS, MV and APES beamformers when imaging point reflectors at a range of approximately 100 m. We have used a simulated environment developed by the Norwegian Defence Research Establishment (FFI), and verified our results from simulations using experimental data from the SX90 sonar. We start by presenting results from the simulations in Section III. A. In Section III. A.1 we illustrate the importance of applying an interpolated array transformation prior to adaptive beamforming, and in Section III. A.2 we evaluate the resolution capabilities of each beamforming method. Finally, we present results from experimental data in Section III. B, comparing the adaptive beamformers to the conventional one and illustrating an improvement in performance which is consistent with the simulations.

A. Simulations

We have designed the simulations to correspond to a possible scenario for a fish finding sonar. The transmitted pulse was a 32 ms linear frequency modulated (FM) chirp with center frequencies ranging from 20 kHz to 30 kHz, corresponding to the operating frequencies of the SX90 sonar. This corresponds to relative radii of 2.47 λ to 3.7 λ, i.e., the relative curvature decreases with increased frequency as the radius of the array becomes larger relative to the wavelength. The transmitted bandwidth was 1 kHz, and we applied a matched filter for pulse compression prior to beamforming. The data was bandpass sampled, yielding complex data samples. The simulation setup consists of a 32-element circular array with a radius of 18.5 cm. The directional response of each circular element is given by Eq. 7. 13 of the 32 elements, covering a sector of 146.25 degrees were used to form each receive beam as illustrated by Fig. 3.

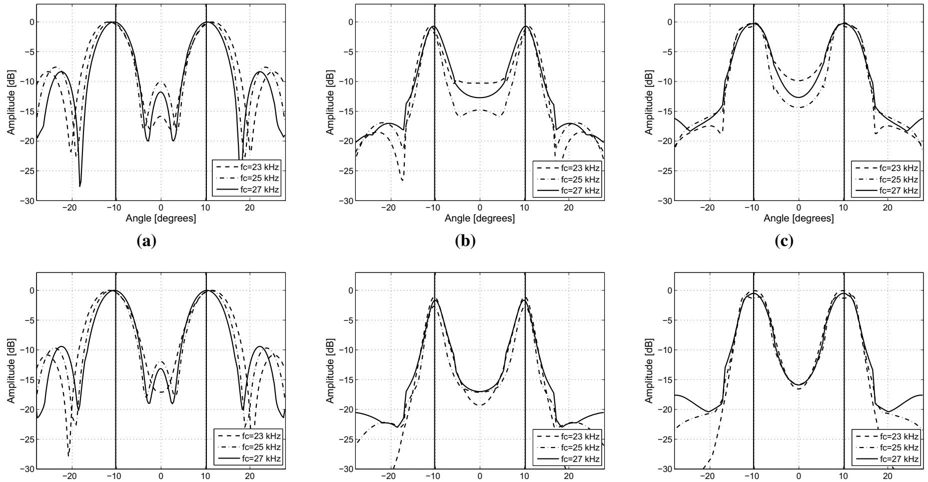

(a) (b) (c)

(d) (e) (f)

Fig. 4: *The upper plots show the steered response for the (a) DAS, (b) MV, and (c) APES beamformers, without applying an interpolated array transformation. The three curves in each plot correspond to center frequencies of 23, 25 and 27 kHz, and the solid vertical lines indicate the DOA of the two point sources. The lower plots show the response for the same beamformers ((d) DAS, (e) MV, (f) APES) with the Friedlander transformation applied. A sector size of 60 degrees was used, and K=12 elements in the virtual array. The plots are normalized by the peak value of the DAS beamformer.*

In the following examples, DAS denotes the uniformly weighted delay-and-sum beamformer, and DAS Hann implies that a Hann window was applied for sidelobe suppression. For the APES and MV beamformers we use a subarray length of $L = 5$ and 3% diagonal loading for added robustness.

1) Effects of the interpolated array transformation: Prior to beamforming, we used the Friedlander transformation to map the data from a curved array to a virtual ULA with $K = 12$ elements using an in-sector of 60 degrees. In Fig. 4, the steered response for the DAS, MV and APES beamformers without applying any transformation prior to beamforming (a-c) is compared to the steered response of the same beamformers when the Friedlander transformation was applied (d-f). The three curves in each plot correspond to center frequencies of 23, 25 and 27 kHz. The DAS beamformer performs similarly with and without the transformation, as expected since there is no processing step which relies on the array geometry. For the adaptive MV and APES beamformers, there is a significant improvement in resolvability when the interpolated array transformation is applied. While the two targets are resolved by about 10 to 14 dB without the transformation (b-c), they are resolved by 15 to 17 dB when the array geometry is properly accounted for (e-f). We also observe a reduction in the sidelobe levels as well as a slightly narrower target response. The slight discontinuities, most visible in (c), are caused by the discrete transitions between imaging sectors.

Since the exact amplitudes are not known, the output from the DAS beamformer is used as a reference when evaluating the beamformers' ability to estimate the signal amplitudes correctly. In Fig. 4, the MV beamformer generally has its peaks at around -1 to -2 dB, while the APES

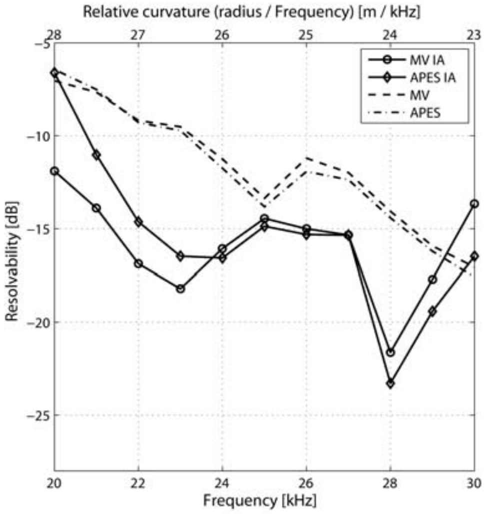

Fig. 5: *Resolvability of two targets with (MV IA, APES IA) and without (MV, APES) the Friedlander transformation applied. The transmitted center frequencies range from 20 kHz to 30 kHz. The relative curvature, defined as radius [m]/frequency [kHz], is indicated along the upper x-axis.*

beamformer has its peaks closer to the reference. This is a result of signal cancellation which affects the MV beamformer more than the APES beamformer. Also, the APES beamformer displays somewhat asymmetric peaks for the 25 kHz case. This effect is not uncommon for the APES beamformer, and is related to the fact that it gives accurate amplitude estimates in the direction of interest, but it may suffer from "false peaks" in other directions [30]. These false peaks seem to appear mainly in idealized scenarios with point reflectors imaged in an environment with little noise.

Figure 5 illustrates the different beamformers' resolvability of the two point sources, defined as the difference, in dB, between the two peaks in Fig. 4 and the saddle point between them. The solid lines show the results when applying the Friedlander transformation prior to beamforming, while the dotted lines correspond to the results without applying any transformation. For most transmit frequencies we see a significant improvement in the resolvability when applying the interpolated array transformation prior to beamforming. At the highest transmit frequency (30 kHz) this is not the case. This is likely to be related to the transformation error, which can be significant at high frequencies where the element spacing of the virtual array is $> \lambda/2$.

Figures 4 and 5 illustrate that although it is possible to apply adaptive beamforming methods directly to a curved array, the performance is degraded. The relatively poor performance without applying an interpolated array transformation is as expected, since subarray averaging is performed on data from a cylindrical array, where each subarray faces a different direction. The result is a smearing of the data, and a reduced ability to place deep nulls in the directions of interfering signals. The results of the interpolated array transformation may be improved by optimizing the interpolation matrix design as discussed in e.g. [31], but that has not been considered in this work. In the remaining results, we apply the Friedlander transformation prior to beamforming unless otherwise stated.

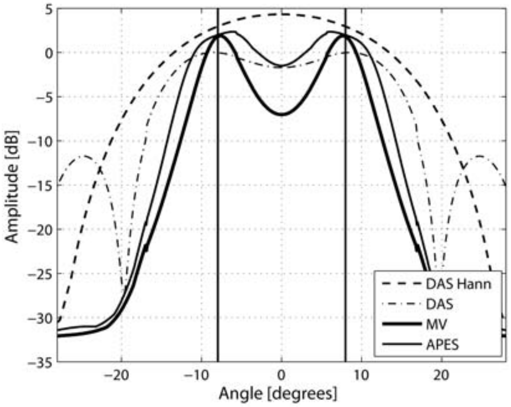

Fig. 6: *Steered response for the DAS, MV and APES beamformers. The transmitted pulse was a 32 ms linear FM chirp with center frequency 22 kHz.*

2) Beamformer resolution capabilities: Figure 6 shows the steered response from two closely spaced point targets imaged using the DAS with uniform weighting, the Hann-weighted DAS, MV and APES beamformers. The two solid lines indicate the DOA of the two point sources. In this case, the DAS with Hann weights is unable to resolve the two targets, while the DAS with uniform weighting barely resolves them by about 2 dB. The MV and APES beamformers resolve the two sources by about 4 and 8 dB, respectively. The peaks for the DAS beamformer appear slightly shifted relative to the DOA of the sources. This effect is caused by constructive interference between the mainlobe from one source and the sidelobe originating from the other source. In Fig. 6, the DAS beamformer appears to under-estimate the signal amplitudes causing the other beamformers to show amplitudes > 0 dB. This effect varies as the source separation is slightly changed, and is likely to be a result of constructive and destructive interference between the mainlobes of one reflector and the sidelobes of the other.

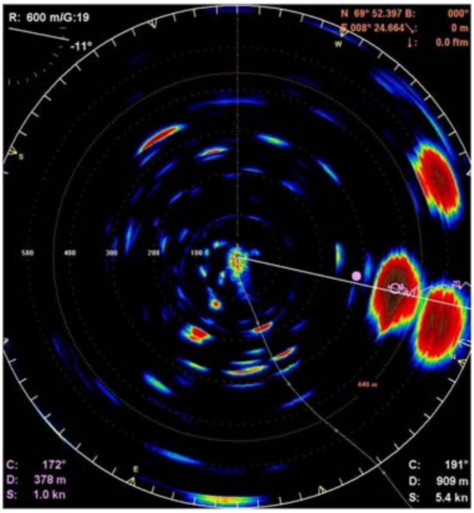

Fig. 7: *Example screen image from the SX90 fish finding sonar. Three herring schools are clearly visible. Courtesy of Kongsberg Maritime.*

B. Experimental results

We have verified the results from simulations using experimental data from the Simrad SX90 sonar; a low frequency, long range fish finding sonar [32]. The SX90 sonar consists of 256 elements configured as a cylinder with a diameter of about 38 cm and a height of 56 cm. Figure 7 shows an example image from the SX90 sonar, with three herring schools clearly visible.

To evaluate the performance of adaptive beamforming applied to experimental data, we use data from controlled experiments. Since the physical array is two-dimensional and cylindrical, we coherently sum the data from each row of the array to synthesize a 32-element cylindrical stave array prior to beamforming. In [33], the authors propose a different approach which involves beamforming each circular row separately before combining the outputs using beamforming for a linear array.

The experimental setup consisted of a corner reflector placed in the water column at 5 m depth and at a range of approximately 100 m. As in the simulations, we used 13 physical elements at a time for beamforming, and mapped the data to a virtual ULA with K=12 elements prior to beamforming. The directional element response vector, $\mathbf{g}$, was approximated by Eq. 7. In total 256 receive beams were formed, covering 360 degrees. For the adaptive MV and APES beamformers, we used a subarray length of L=5 and 3% diagonal loading for added robustness. We applied a Hann window for sidelobe suppression when using the conventional DAS beamformer. In many practical applications the un-weighted DAS beamformer is avoided because of its high sidelobe levels.

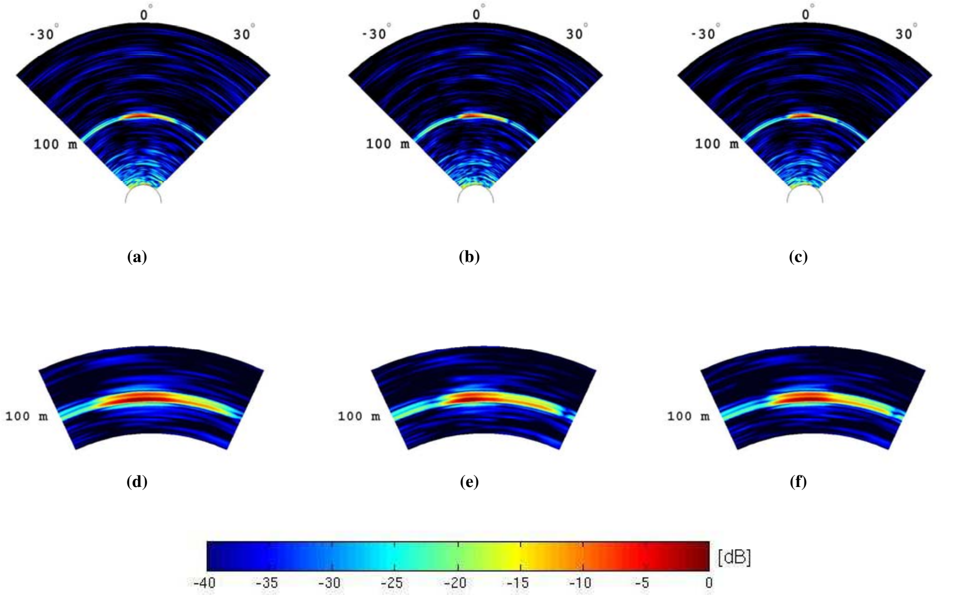

(a) (b) (c)

(d) (e) (f)

Fig. 8: *Experimental results using data from the SX90 sonar, when imaging a corner reflector at a range of 104 m. The Hann-weighted DAS beamformer (left) is compared to the MV (middle) and APES (right) beamformers. (a)-(c) show a 90-degree sector with the corner reflector in the middle. (d)-(f) show a small region around the reflector from a range of 80 m to 120 m covering a 50-degree sector. The transmitted pulse is a 32 ms weighted linear FM chirp with center frequency 27 kHz and a bandwidth of 700 Hz. Each image is normalized by its peak value.*

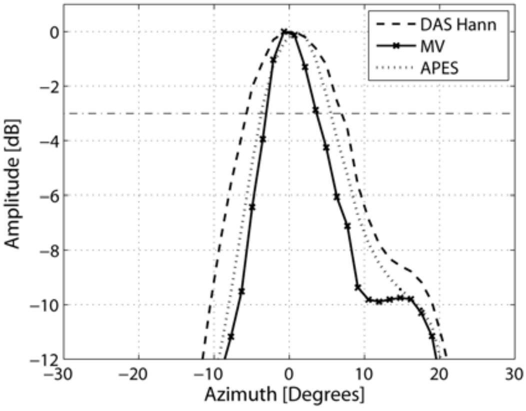

Fig. 9: *Slice through the center of the corner reflector using the DAS, MV and APES beamformers, respectively.*

Figure 8 shows the beamformed images created using data from a single ping. The top images show a 90-degree sector and a range of 0 to 200 m, while the bottom images show a smaller region covering a 60-degree sector around the target and a range span of 80 to 120 m. The target was located at a range of approximately 104 m, and the transmitted pulse was a 32 ms linear FM chirp with 700 Hz bandwidth and a center frequency of 27 kHz. Each image is normalised by its peak value and plotted using a logarithmic scale.

The improvement in azimuth resolution is most visible when looking at a slice through the reflector at 104 meters, as shown in Fig. 9. The -3dB mark is indicated by a dashed line and used to define the beamformers' azimuth resolution. In this case the MV beamformer offers an improvement of about 45% in the -3dB width compared to the conventional DAS beamformer, while the APES beamformers offers an improvement of about 30%.

Figure 10 shows images from three additional selected pings with different transmit pulses. The left column contains images created using the DAS with a Hann window (top), the MV (middle) and the APES (bottom) beamformers, when transmitting a 16 ms linear FM chirp at a center frequency of 27 kHz and with a 700 Hz bandwidth. The images in the middle column show the beamformed images when transmitting a 32 ms pulse at a center frequency of 27 kHz and with a bandwidth of 300 Hz. In the rightmost column, the transmitted pulse was a 36 ms pulse with a center frequency of 26 kHz and a bandwidth of 500 Hz. In the latter case a double target was located at a range of about 90 m. The resolution capabilities and sidelobe levels of each of the beamformers is illustrated by slices through each imaged target, at the bottom of Fig. 10.

In all four cases, the adaptive beamformers display sidelobe levels comparable to those of the conventional DAS beamformer with a Hann window applied for sidelobe suppression, as well as a significant improvement in azimuth resolution. For the double target in the right column of Fig. 10, the separation of the two sources is significantly improved by both of the adaptive beamformers. The background amplitude levels in areas without any strong reflectors are similar for the adaptive and conventional beamformers. The results on experimental data are in good agreement with the simulations. The improvement in azimuth resolution when using experimental data is somewhat less than the observed improvement in the noise-free simulations. Still, the improvement when using experimental data is in the range of 40 to 50% for the MV beamformer and 20 to 30% for the APES beamformer.

In some scenarios we observe a "ghost" reflection directly after the main reflection in the range direction, as in Fig. 8. This is likely to be caused by multipath propagation where the pulse is reflected by the corner reflector via the sea surface back to the sonar.

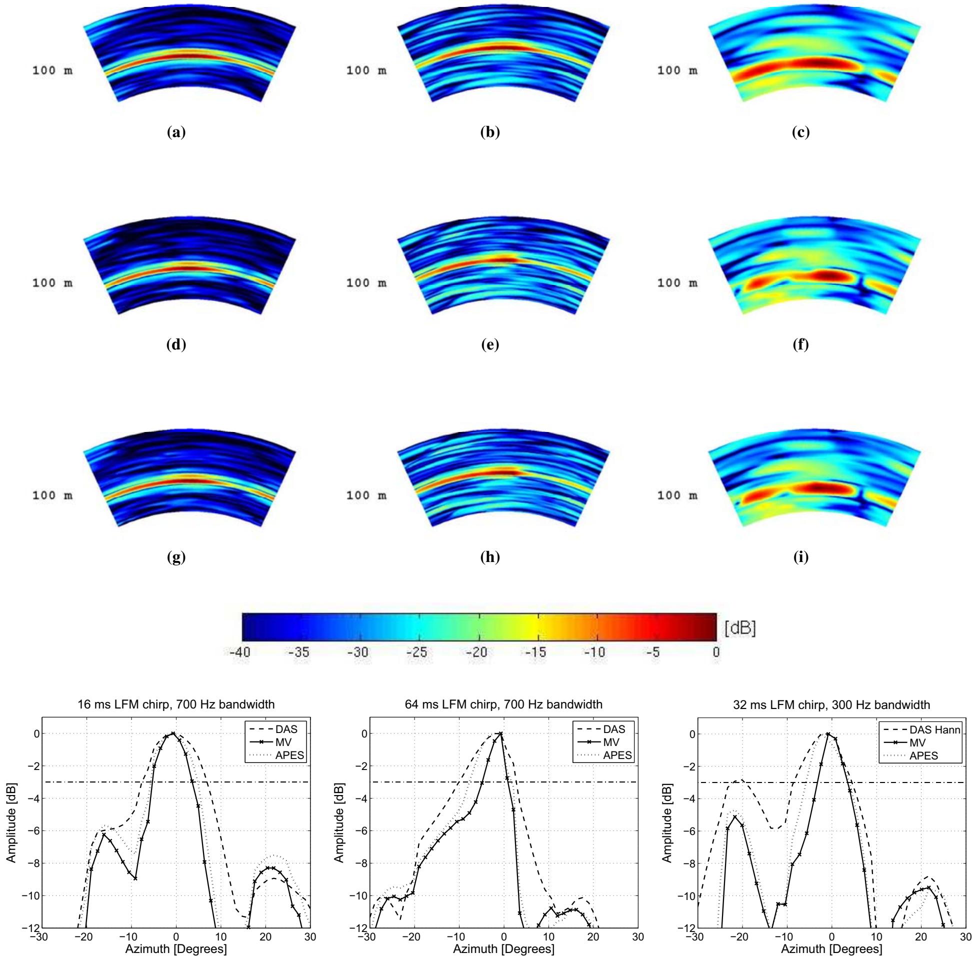

Fig. 10: *Experimental results from three different cases, each vertical column corresponding to a different case. Each row compares the Hann-weighted DAS beamformer (a)-(c) to the MV beamformer (d)-(f) and the APES beamformer (g)-(i). In the left column, the transmitted pulse was a 16 ms linear FM chirp with a center frequency of 27 kHz and a bandwidth of 700 Hz. The middle column shows the results when transmitting a 64 ms linear FM chirp with a center frequency of 27 kHz and a bandwidth of 700 Hz. In the right column, the transmitted pulse was a 32 ms linear FM chirp with a center frequency of 27 kHz and a bandwidth of 300 Hz. Each image spans a 50-degree sector and a range span from 80 m to 120 m. Each image is normalized by its peak value. The bottom plots show slices through the imaged reflector for each case. The -3 dB mark is indicated by a dashed line.*

IV. Summary

We have applied adaptive beamforming using the MV and APES beamformers to sonar imaging in an active environment with highly correlated sources, using a cylindrical array. A key step when using adaptive beamformers in an active sonar system is subarray averaging. Without subarray averaging, signal cancellation can cause severe underestimation of the signal amplitudes, an effect which is problematic in imaging applications. We have used the interpolated array approach proposed by Friedlander to transform the steering vector of the curved array to a Vandermonde structure suitable for subarray averaging prior to beamforming. Through simulations, we illustrate the importance of applying such a transformation.

Results from simulations show that the MV and APES beamformers outperform the conventional DAS beamformer with respect to mainlobe width and the ability to resolve two closely spaced targets. Further, both adaptive methods offer sidelobe levels comparable to those of the DAS with a Hann window applied for sidelobe suppression. The MV beamformer offers higher azimuth resolution than the APES beamformer, while the latter offers slightly more reliable amplitude estimates.

We have verified the results from simulations using experimental data from the Simrad SX90 sonar. When imaging a corner reflector placed in the water column, we observe a significant improvement in azimuth resolution, and sidelobe levels comparable to those of the conventional beamformer weighted with a Hann window. When using the adaptive MV beamformer the observed improvement in azimuth resolution is about 40 to 50% compared to the conventional method. For the APES beamformer the improvement is in the range of 20 to 30%.

In conclusion, adaptive beamformers perform well on experimental sonar data for fish finding applications. The MV beamformer in particular, offers a significant improvement in azimuth resolution while maintaining the low sidelobe levels of a weighted conventional beamformer. These advantages come at the cost of added computational complexity.

V. Acknowledgements

We kindly thank Kongsberg Maritime for providing experimental data from the Simrad SX90 sonar. We also acknowledge Torstein O. Sæbø from the Norwegian Defence Research Establishment for assistance in the simulations, Even B. Lunde for helpful input and discussions, and Professor Sverre Holm for his contributions to this work. This work was carried out as a part of the Norwegian Research Council project High Resolution Beamforming and Imaging (project no: 182742).

Bibliography

[1] D. H. Johnson and D. E. Dudgeon, *Array Signal Processing: Concepts and Techniques.* Prentice Hall, 1992.

[2] F. Bryn, "Optimum signal processing of three-dimensional arrays operating on gaussian signals and noise," *J. of the Acoustical Society of America*, vol. 34, no. 3, pp. 289–297, Mar 1962.

[3] J. Capon, "High-resolution frequency-wavenumber spectrum analysis," *Proc. IEEE*, no. 8, pp. 1408–1418, August 1969.

[4] H. Krim and M. Viberg, "Two decades of array signal processing research: The parametric approach," *IEEE Signal Process. Mag.*, vol. 13, no. 4, pp. 67–94, Jul 1996.

[5] J. E. Hudson, *Adaptive array principles.* P. Peregrinus LTD. on behalf of the Institution of Electrical Engineers, 1981.

[6] N. L. Owsley, "Systolic array adaptive beamforming," Naval Underwater Systems Center, Tech. Rep., Sept 1987.

[7] S. Stergiopoulos, "Implementation of adaptive and synthetic-aperture processing schemes in integrated active-passive sonar systems," *Proc. IEEE*, vol. 86, no. 2, pp. 358 –398, Feb. 1998.

[8] ——, *Handbook on Advanced Signal Processing for Sonar, Radar and Non-Invasive Medical Diagnostic Systems*, 2nd ed. Boca Raton, FL, USA: CRC Press LLC, Mar 2000, ch. Advanced Beamformers, pp. 79–146.

[9] T.-J. Shan and T. Kailath, "Adaptive beamforming for coherent signals and interference," *IEEE Trans. Acoust., Speech, Signal Process.*, pp. 527–536, Jun 1985.

[10] K. Lo, "Adaptive array processing for wide-band active sonars," *IEEE J. Oceanic Eng.*, vol. 29, no. 3, pp. 837 – 846, Jul. 2004.

[11] G. Cook, B. Lau, and Y. Leung, "An alternative approach to interpolated array processing for uniform circular arrays," in *Circuits and Systems, 2002. APCCAS '02. 2002 Asia-Pacific Conference on*, vol. 1, 2002.

[12] T. Bronez, "Sector interpolation of non-uniform arrays for efficient high resolution bearing estimation," in *Acoustics, Speech, and Signal Processing, 1988. ICASSP-88., 1988 International Conference on*, vol. 5, Apr. 1988, pp. 2885–2888.

[13] B. Friedlander, "Direction finding using an interpolated array," in *Proc. IEEE Int. Conf. Acoust., Speech and Signal Proc.*, vol. 5, apr 1990, pp. 2951 –2954.

[14] A. Weiss and M. Gavish, "Direction finding using ESPRIT with interpolated arrays," *IEEE Trans. Signal Process.*, vol. 39, pp. 1473–1478, jun 1991.

[15] A. Weiss, B. Friedlander, and P. Stoica, "Direction-of-arrival estimation using mode with interpolated arrays," *Signal Processing, IEEE Transactions on*, vol. 43, no. 1, pp. 296 –300, jan 1995.

[16] B. Lau, G. Cook, and Y. Leung, "An improved array interpolation approach to doa estimation in correlated signal environments," in *Proc. IEEE Int. Conf. Acoust., Speech and Signal Proc.*, vol. 2, may 2004, pp. 237–240.

[17] P. Yang, F. Yang, and Z. P. Nie, "DOA estimation with sub-array divided technique and interpolated ESPRIT algorithm on a cylindrical conformal array antenna," *Progress in Electromagnetics Research (PIER)*, vol. 103, pp. 201–216, 2010.

[18] D. V. Sidorovich and A. B. Gershman, "Two-dimensional wideband interpolated Root-MUSIC applied to measured seismic data," *IEEE Trans. Signal Process.*, vol. 46, pp. 2263–2267, Aug. 1998.

[19] P. Yang, F. Yang, and Z. P. Nie, "Robust adaptive beamformer using interpolation technique for conformal antenna array," *Progress in Electromagnetics Research (PIER)*, vol. 23, pp. 215–228, 2010.

[20] B. K. Lau, "Applications of adaptive antennas in third-generation mobile communications systems," Ph.D. dissertation, Curtin University of Technology, 2002.

[21] A. Albert, *Regression and the Moore-Penrose Pseudoinverse*. New York: Academic Press, 1972.

[22] H. L. Van Trees, *Detection, estimation and modulation theory IV: Otpimum Array Processing*. John Wiley and Sons, Inc., 2003.

[23] B. Widrow, K. Duvall, R. Gooch, and W. Newman, "Signal cancellation phenomena in adaptive antennas: Causes and cures," *IEEE Trans. Antennas Propag.*, vol. 33, no. 3, pp. 469–478, May 1982.

[24] J.-F. Synnevåg, "Adaptive beamforming for medical ultrasound imaging," Ph.D. dissertation, University of Oslo, 2009.

[25] J.-F. Synnevåg, A. Austeng, and S. Holm, "Benefits of minimum variance beamformning in medical ultrasound imaging," *IEEE Trans. Ultrason., Ferroelectr., Freq. Control*, Sept 2009.

[26] ——, "Adaptive beamforming applied to medical ultrasound imaging," *IEEE Trans. Ultrason., Ferroelectr., Freq. Control*, pp. 1606–1613, August 2007.

[27] H. Cox, R. Zeskind, and M. Owen, "Robust adaptive beamforming," *IEEE Trans. Acoust., Speech, Signal Process.*, vol. 35, no. 10, pp. 1365 – 1376, Oct. 1987.

[28] B. D. Carlson, "Covariance matrix estimation errors and diagonal loading in adaptive arrays," *IEEE Trans. Aerosp. Electron. Syst.*, vol. 24, no. 4, pp. 397–401, Jul 1988.

[29] P. Stoica, H. Li, and J. Li, "A new derivation of the APES filter," *IEEE Signal Process. Lett.*, vol. 6, no. 8, pp. 205 –206, Aug. 1999.

[30] A. Jakobsson and P. Stoica, "Combining Capon and APES for estimation of spectral lines," in *Circuits, Systems, and Signal Processing*, vol. 19, no. 2, 1999, pp. 159–169.

[31] P. Hyberg, M. Jansson, and B. Ottertsen, "Array mapping: Optimal transformation matrix design," *IEEE Trans. Acoust., Speech, Signal Process.*, vol. 3, pp. 2905–2908, August 2002.

[32] *Simrad SX90 low frequency sonar brochure [online]*, Available at: http://www.simrad.com.

[33] S. Stergiopoulos and A. Dhanantwari, "Implementation of adaptive processing in integrated active-passive sonars with multi-dimensional arrays," in *Advances in Digital Filtering and Signal Processing, 1998 IEEE Symposium on*, jun 1998, pp. 62 –66.

Paper III

Improving Sonar Performance in Shallow Water using Adaptive Beamforming

A. E. A. Blomberg, A. Austeng, R. E. Hansen and S. A. V. Synnes

IEEE Journal of Oceanic Engineering
Revised version submitted Aug. 30, 2011.

Paper IV

Improved Interferometric Sonar Performance in Shallow Water using Adaptive Beamforming

A. E. A. Blomberg, R. E. Hansen, S. A. V. Synnes and A. Austeng

Proceedings of underwater acoustic measurements (UAM)
Kos, Greece, June 2011.

Improved Interferometric Sonar Performance in Shallow Water using Adaptive Beamforming

A. E. A. Blomberg, R. E. Hansen, S. A. V. Synnes and A. Austeng

Abstract *–* The effective range of a sonar depends on the environment in which it is operating. In an environment with high background noise or considerable multipath, the signal-to-noise ratio (SNR) is low and the range limited. Multipath propagation is often severe in shallow waters. In this work we increase the interferometric coherence and hence the useful imaging range by suppressing multipath signals using a low complexity adaptive (LCA) beamformer. We use data from the NATO Undersea Research Centre (NURC) collected during the MASAI02 trial. In our analysis we select a sub-set of the 256 available elements and create an interferometer with 2 and 3 elements in each receiver array. Our results show a consistent improvement in the interferometric coherence when using adaptive LCA beamforming as opposed to conventional beamforming. This implies an improvement in the SNR and an increase in the useful imaging range. The greatest improvements are observed when the prediction model indicates that there are strong multipath signals arriving from an angle well separable from the direct return.

I. Introduction

In shallow water environments, the performance of side scan sonar and synthetic aperture sonar (SAS) is often degraded because of multipath propagation [1]. The multipath signals interfere with the direct return causing the signal-to-noise ratio (SNR) to drop.

An interferometric sonar uses the phase difference between two vertically displaced receivers to estimate the relative depth of the seafloor. In the presence of multipath, the depth estimates may be unreliable since the assumption of a single echo arriving at each range sample is violated. In this study the aim is to improve interferometric sonar performance by reducing the multipath interference at each receiver array through adaptive beamforming. The beamformed output from the two receivers can then be used to compute the interferogram. An estimate of the SNR in a single ping can be derived from the interferometric coherence between the time series received at the two receivers [2,3]. Based on this relation we use the interferometric coherence as a performance metric when evaluating the different beamformers' ability to suppress interfering multipath signals. Focusing on the use of small receiver arrays suitable for mounting on a towed platform, we conclude that the low complexity adaptive (LCA) beamformer presented in [4] gives a consistent improvement in the coherence and an increase in the effective sonar range.

II. Experimental setup

This study is based on sonar data collected by NATO Undersea Research Centre (NURC) in 2002 [5]. The data was collected in an area near La Spezia, Italy, where the water depth was about 20 m. In the experiment, a 100 kHz sonar was mounted on a 10.7 m high tower resting on the seafloor. The sonar array consisted of 256 vertically displaced elements with $\lambda/2$ spacing, with the 64 center elements forming a fully programmable transmitter. The transmitted pulse was a linear FM chirp with a bandwidth of 10 kHz. Further details about the Multi Aspect Synthetic Aperture sonar Imaging (MASAI) system can be found in [6].

We use a subset of the available receivers, creating an interferometric array with 2-3 elements in each receiving array. The receiving arrays are separated by a baseline of 9 λ. The transmitted beam used in this study is a narrow beam focused at medium range. Figure 1 illustrates the sonar geometry.

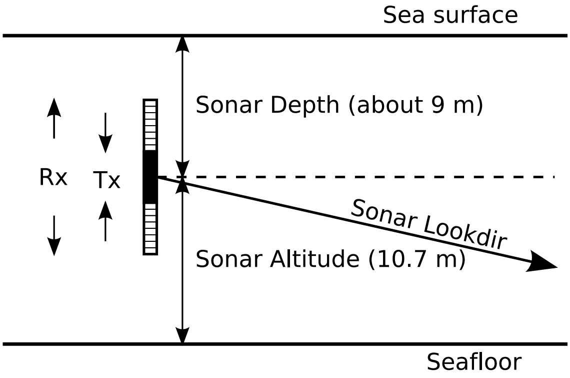

Fig. 1: *Sonar geometry.*

III. Multipath prediction

For bottom imaging applications the SNR can be expressed as the ratio between the desired direct return and the sum of all multipath contributions and background noise. Each multipath describes a round-trip propagation from the transmitter into the medium and back to the receiver. We have used the sonar performance model described in [7] to estimate the contribution of each multipath.

Figure 2 (top) shows a beamformed image created using data from the experimental setting described in Section II. The image was constructed by steering the receive beam consecutively in directions between -45 and 45 degrees relative to the horizontal, creating an image of the desired direct echo from the seafloor as well as the multipath signals. A 100-element receiver array was used to create the beamformed image. The direct return and the most significant predicted multipaths are indicated by solid lines on top of the beamformed image in Fig. 2 (top). The predicted intensity of each multipath as a function of range is shown in Fig. 2 (bottom). We have adopted the same naming convention for multipaths as in [5], combining the letter ’b’ for bottom scatterings and ’s’ for surface scatterings, using lowercase letters for specular reflections and an uppercase letter for the single non-specular scattering. The dominating multipath for the entire imaging range is the one labeled ’Bs’. As the name indicates, it has a path which is reflected off the seafloor, up to the sea surface and back toward the receiver. It arrives with an angle well separable from that of the direct return. Depending on the beamwidth of the receiver, it may still interfere significantly with the direct return, particularly at far range.

IV. Receive beamforming

The conventional delay-and-sum (DAS) beamformer applies a delay to each receiver element to steer the beam in a given direction [8]. A set of pre-defined sensor weights are applied before coherently combining the signals from each sensor. Adaptive beamformers use the statis-

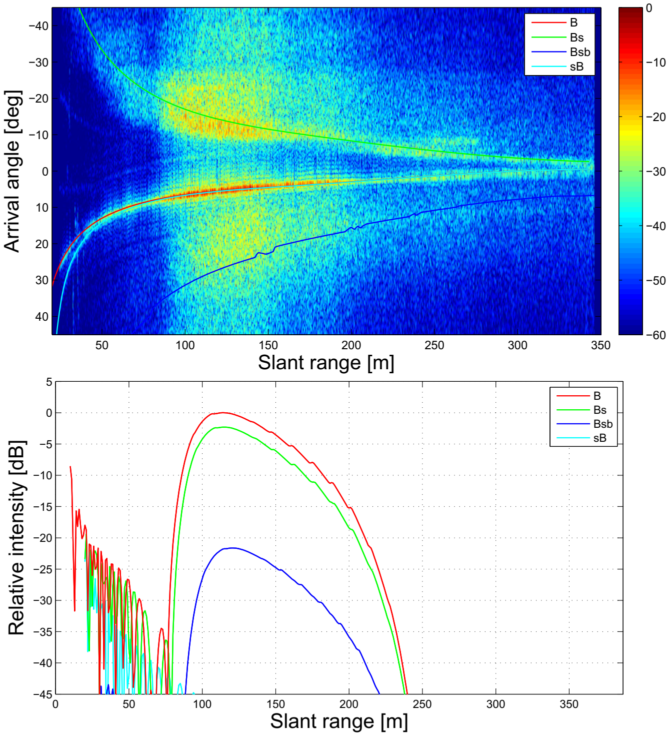

Fig. 2: *Top: Beamformed image of the direct return and multipaths as a function of slant range and direction of arrival. Bottom: Modeled intensity of the direct return, 'B', and the most significant multipaths.*

tics of the received data to compute a set of weights which are optimal in some sense, for each image pixel. They are generally computationally intensive and require techniques such as spatial smoothing for robustness. The minimum variance (MV) beamformer [9] is well known for its high resolution and interference suppression capabilities. However, the need for spatial smoothing when applied to an active imaging system [10] makes it sub-optimal when using a receiver array with very few elements. The spatial smoothing step requires at least three receiver elements.

In [4], Synnevåg et. al propose a simple and robust adaptive beamformer; the low complexity adaptive beamformer (LCA), where the sensor weights are chosen from a set of P pre-defined complex windows instead of allowing full adaptivity. The LCA is based on the same criterion as the MV beamformer, choosing the window function $\mathbf{w}$ that minimizes the cost function:

$$\min_{p} E\left\{|\mathbf{w}_p\mathbf{y}[n]|^2\right\}, \tag{1}$$

where $\mathbf{y}$ is the output from the receiver array after pre-steering using a time delay. In practice, Eq. 1 can be estimated by minimizing $|\mathbf{w}_p^H\mathbf{y}|$ for each range and steering angle. Each window function is normalized such that the sum of the weights equals 1, ensuring a distortionless response in the steering direction. To avoid rapid variations in the choice of window functions, we use an observation period of one pulse length. The optimal window will not vary considerably during such a short period since the directions of arrival of the direct return and multipaths are slowly varying. For each range sample, we apply the window function which is most frequently chosen within the observation period.

A key step in the LCA beamformer is choosing a sensible set of pre-defined window functions. We use rectangular and Hanning windows, and allow windows with an asymmetrical response as the ones often chosen by the MV beamformer. These windows are created by shifting the response by ϕ, i.e., multiplying the window function $\mathbf{w}$ by $e^{j\phi}$. The maximum shift is limited to one sixth of the mainlobe width. Table I lists the set of pre-defined windows we have chosen, 'BW' denoting the two-sided -3 dB width of the beampattern of a rectangular window.

Table I: *Pre-defined window functions.*

Type	Steering angle, ϕ
Rectangular	0, ±1/6 BW, ±1/12 BW, ±1/24 BW, ±1/48 BW
Hanning	0 ±1/6 BW, ±1/12 BW, ±1/24 BW, ±1/48 BW

V. RESULTS

Figure 3 (upper plot) shows the measured interferometric coherence when using two elements in each receiver array and beamforming toward the seafloor. The point where the coherence drops below 2/3 is defined as the maximum achievable range and marked by a solid horizontal line. The conventional un-weighted and Hanning-weighted DAS beamformers overlap in the two-element case. They both drop below the 2/3 mark at 75 meters where there is a dip in the coherence, and again at 105 meters. The LCA beamformer displays an over-all higher coherence because of its ability to suppress multipath interference. It drops below the 2/3 mark for the first time at 120 meters.

In Fig. 3 (lower plot), we show the corresponding results when using three elements in each receiver array. The coherence has improved for all beamformers as a result of the narrower receiver response and increased array gain of using three instead of two elements in each receiver. The Hanning-weighted DAS beamformer performs poorly compared to the other beamformers because of its wide response. Although the un-weighted DAS has higher sidelobe levels, it is preferred because of its relatively narrow response. The LCA beamformer outperforms the conventional beamformers because of its ability to choose between a set of window functions. In this setting, the LCA beamformer typically chooses rectangular windows (i.e., equal weighting over all receivers), steered to one side in order to suppress interfering multipaths. The interfering multipath in this case is 'Bs', as indicated by Fig. 2 (bottom). Although it arrives at an angle which is well separable from the direct return, it interferes with the direct return because of the wide response of the 2- and 3- element receivers.

Beamforming toward the sea floor requires *a priori* information about the water depth. We extract this information from the beamformed image in Fig. 2 (top). For real-time interferometric measurements, the local depth may be estimated using data from the previous ping.

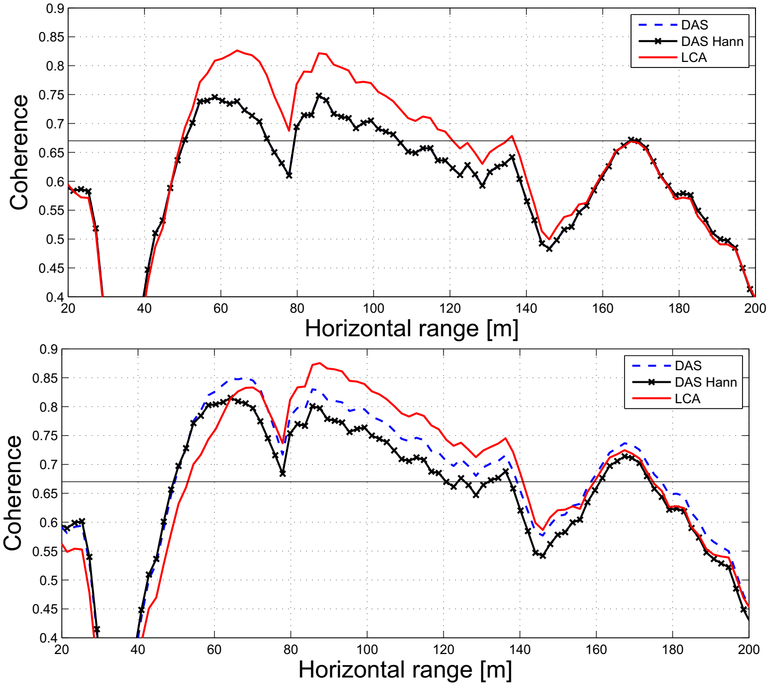

Fig. 3: *Interferometric coherence for the different beamformers using two (upper plot) and three (lower plot) elements in each receiving array.*

VI. Conclusions

We conclude that the adaptive LCA beamformer can be used to improve the interferometric coherence and hence the useful imaging range, for small receiver arrays in a shallow water environment. The increase in performance depends on the amount of multipath and the direction from which it is arriving. In challenging environments, a small improvement in the coherence may imply a significant increase in the achievable imaging range.

VII. Acknowledgments

We wish to thank the NATO Undersea Research Centre (NURC) for providing the experimental data. In particular, we thank Marc Pinto, Andrea Bellettini, and Johannes Groen at NURC. In addition, we thank Anthony Lyons at Applied Research Laboratory, Pennsylvania State University and Torstein O. Sæbø at the Norwegian Defence Research Establishment (FFI) for fruitful inputs and discussions.

Bibliography

[1] B. J. Davis, P. T. Gough, and B. R. Hunt, "Modeling surface multipath effects in synthetic aperture sonar," *IEEE J. Oceanic Eng.*, vol. 34, no. 3, pp. 239–249, July 2009.

[2] H. Zebker and J. Villasenor, "Decorrelation in interferometric radar echoes," *Geoscience and Remote Sensing, IEEE Transactions on*, vol. 30, no. 5, pp. 950 –959, September 1992.

[3] S. A. V. Synnes, R. E. Hansen, and T. O. Sæbø, "Assessment of shallow water performance using interferometric sonar coherence," in *Proceedings of Underwater Acoustic Measurements 2009*, Nafplion, Greece, June 2009.

[4] J.-F. Synnevåg, S. Holm, and A. Austeng, "A low complexity data-dependent beamformer," in *Ultrasonics Symposium, 2008. IUS 2008. IEEE*, 2008, pp. 1084 –1087.

[5] A. Bellettini, M. A. Pinto, and L. Wang, "Effect of multipath on synthetic aperture sonar," in *Proceedings of World Congress on Ultrasonics WCU 2003*, Paris, France, September 2003.

[6] L. Wang, G. Davies, A. Bellettini, and M. Pinto, "Multipath effect on DPCA micronavigation of a synthetic aperture sonar," in *Impact of Littoral Environmental Variability on Acoustic Predictions and Sonar Performance*, N. G. Pace and F. B. Jensen, Eds. Italy: Kluwer Academic Publishers, 2002, pp. 465–472.

[7] S. A. V. Synnes, "Shallow water sonar performance modelling," Norwegian Defence Research Establishment (FFI), Tech. Rep., in print.

[8] D. H. Johnson and D. E. Dudgeon, *Array signal processing: Concepts and Techniques*, ser. Signal processing series. Englewood Cliffs, NJ, USA: Prentice Hall, 1993.

[9] J. Capon, "High-resolution frequancy-wavenumber spectrum analysis," *Proc. IEEE*, no. 8, pp. 1408–1418, August 1969.

[10] T.-J. Shan and T. Kailath, "Adaptive beamforming for coherent signals and interference," *IEEE Trans. Acoust., Speech, Signal Process.*, pp. 527–536, June 1985.

Paper V

Adaptive Sonar Imaging using Aperture Coherence

A. E. A. Blomberg, C.-I. C. Nilsen, A. Austeng and R. E. Hansen

IEEE Journal of Oceanic Engineering
Submitted Oct. 1, 2011.